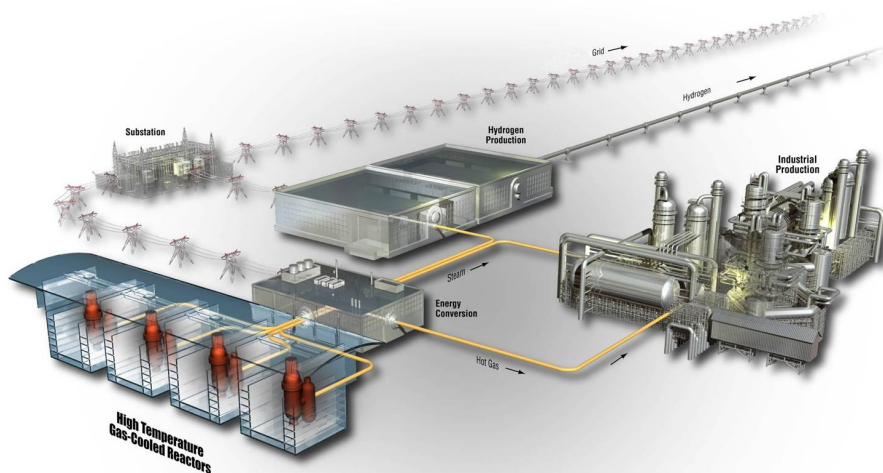


AGR-1 Fuel Compact 6-3-2 Post- Irradiation Examination Results

Paul Demkowicz, Jason Harp,
Philip Winston, Scott Ploger

December 2012

The INL is a
U.S. Department of Energy
National Laboratory
operated by
Battelle Energy Alliance



DISCLAIMER

This information was prepared as an account of work sponsored by an agency of the U.S. Government. Neither the U.S. Government nor any agency thereof, nor any of their employees, makes any warranty, expressed or implied, or assumes any legal liability or responsibility for the accuracy, completeness, or usefulness, of any information, apparatus, product, or process disclosed, or represents that its use would not infringe privately owned rights. References herein to any specific commercial product, process, or service by trade name, trade mark, manufacturer, or otherwise, does not necessarily constitute or imply its endorsement, recommendation, or favoring by the U.S. Government or any agency thereof. The views and opinions of authors expressed herein do not necessarily state or reflect those of the U.S. Government or any agency thereof.

AGR-1 Fuel Compact 6-3-2 Post-Irradiation Examination Results

**Paul Demkowicz, Jason Harp,
Philip Winston, Scott Ploger**

December 2012

**Idaho National Laboratory
Next Generation Nuclear Plant Project
Idaho Falls, Idaho 83415**

<http://www.inl.gov>

**Prepared for the
U.S. Department of Energy
Office of Nuclear Energy
Under DOE Idaho Operations Office
Contract DE-AC07-05ID14517**

Next Generation Nuclear Plant Project

AGR-1 Fuel Compact 6-3-2 Post-Irradiation Examination Results

INL/EXT-12-27123

December 2012


Approved by:



Paul Demkowicz
VHTR Fuels Post-Irradiation Technical Lead

12/13/12


Date



Jack Simonds
VHTR Fuels Development and Qualification Project
Manager

12/13/2012

Date



David Jensen
VHTR Research and Development Quality Assurance

12/13/2012

Date



David Petti
VHTR Research and Development Director

12/13/2012

Date

SUMMARY

Destructive post-irradiation examination was performed on fuel Compact 6-3-2, which was irradiated in the AGR-1 experiment to a final compact average burnup of 11.3% FIMA (fissions per initial metal atom) and a time-average, volume-average temperature of 1070°C. The analysis of this compact was focused on characterizing the extent of fission product release from the particles and examining particles to determine the condition of the kernels and coating layers. The work included deconsolidation of the compact and leach-burn-leach analysis, visual inspection and gamma counting of individual particles, measurement of fuel burnup by several methods, metallurgical preparation of selected particles, and examination of particle cross-sections with optical microscopy.

A single particle with a defective SiC layer was identified during deconsolidation-leach-burn-leach analysis, which correlates with previous measurements showing elevated cesium in the Capsule 6 graphite fuel holder associated with this fuel compact. The fraction of the europium inventory released from the particles and retained in the compact matrix was relatively high (approximately 6×10^{-3}), indicating release from intact particle coatings. The Ag-110m inventory in individual particles exhibited a very broad distribution, with some particles retaining 80-90% of the predicted inventory and others retaining less than 25%. The average degree of Ag-110m retention in 60 gamma counted particles was approximately 50%. This elevated silver release is in agreement with analysis of silver on the Capsule 6 components, which indicated an average release of 38% of the Capsule 6 inventory from the fuel compacts. In spite of the relatively high degree of silver release from the particles, virtually none of the Ag-110m released was found in the compact matrix, and presumably migrated out of the compact and was deposited on the irradiation capsule components. Release of all other fission products from the particles appears to be less than a single particle equivalent inventory.

Burnup measurements based on gamma spectrometry of individual particles and mass spectrometry of dissolved fuel kernels were in very good agreement (11.0% and 10.7% FIMA, respectively), and were also in good agreement with measurements based on previous gamma spectrometry measurements of the whole compact (11.0% FIMA) and the predicted burnup based on physics simulations of the AGR-1 irradiation (11.3% FIMA).

Ceramographic examination of particle cross-sections revealed that particles exhibited a diverse array of behaviors with respect to the buffer-inner pyrolytic carbon (IPyC) interface, ranging from a fully intact interface, to partial debonding, to complete debonding. The buffer layers in approximately 40% of the particles fractured during irradiation, with the fractures sometimes associated with IPyC fractures. No irradiation-induced damage was noted in the SiC layers of any particles examined. Kernels often protruded into the gaps caused by buffer fracture.

ACKNOWLEDGEMENTS

The valuable contributions of numerous INL staff members in performing experimental work and data analysis are acknowledged. This includes: Dennis Brough (performing deconsolidation-leach-burn-leach analysis, particle inspection, and particle gamma counting); Jeffrey Berg (technical direction and data analysis of deconsolidation-leach-burn-leach results); Dr. Christopher McGrath (data analysis of particle gamma counting data); Dr. Jeffrey Giglio (inductively coupled plasma mass spectroscopy experiments and data analysis); and Brian Frickey and Cad Christensen (preparation of ceramographic mounts).

CONTENTS

SUMMARY	v
ACKNOWLEDGEMENTS	vii
ACRONYMS	xiii
1. INTRODUCTION	1
1.1 Background	1
1.2 Compact 6-3-2 PIE objectives and overview	2
2. DECONSOLIDATION-LEACH-BURN-LEACH	4
3. PARTICLE INSPECTION AND IRRADIATED MICROSPHERE GAMMA ANALYSIS	9
3.1 Visual inspection	9
3.2 Irradiated microsphere gamma analysis	10
4. BURNUP ANALYSIS	20
5. MICROSCOPY	21
5.1 Sample Preparation and Ceramography	21
5.1.1 Mount 21T	21
5.1.2 Mount 22T	25
5.1.3 Mounts 47T and 48T	27
5.1.4 Summary Observations on Compact 6-3-2 Particles	30
5.2 Electron microscopy	31
6. RESULTS SUMMARY	32
7. LESSONS LEARNED AND RECOMMENDATIONS	33
8. REFERENCES	34
Appendix A Deconsolidation-Leach-Burn-Leach Procedure	36
Appendix B Particle Inspection and Irradiated Microsphere Gamma Analysis	41
Appendix C Burnup Measurements	46
Appendix D Ceramographic Morphology Classification	49

FIGURES

Figure 1. Photograph (left) and x-radiograph (right) of an unirradiated AGR-1 fuel compact. Uranium oxide-uranium carbide kernels and non-fueled end caps are clearly visible in the x-radiograph	2
Figure 2. PIE flow chart for Compact 6-3-2	3

Figure 3. Deconsolidation in Cell 5 showing particles dropping down from compact and accumulating on thimble frit.	4
Figure 4. Increased turbidity toward the end of deconsolidation.	5
Figure 5. Highly turbid solution at end of deconsolidation.	5
Figure 6. Deconsolidated particles and residual matrix debris from Compact 6-3-2.	9
Figure 7. Representative photographs of Compact 6-3-2 particles during visual inspection following the second post-burn leach.	10
Figure 8. Normalized Ce-144 activity distribution for 60 particles from irradiated Compact 6-3-2.	13
Figure 9. Normalized Cs-137 activity distribution for 60 particles from irradiated Compact 6-3-2.	14
Figure 10. Normalized Cs-137/Ce-144 activity ratio distribution for 60 particles from irradiated Compact 6-3-2.	14
Figure 11. Normalized Ag-110m/Cs-137 activity ratio for Compact 6-3-2. The MDA was used for particles with no measureable Ag-110m activity. These data are plotted separately in red.	15
Figure 12. Distribution of the measured-to-calculated Ag-110m activity ratio for irradiated Compact 6-3-2 particles.	16
Figure 13. Normalized Eu-154/Cs-137 activity ratio distribution for 60 particles from irradiated Compact 6-3-2.	17
Figure 14. Normalized Ru-106/Cs-137 activity ratio for 60 particles from irradiated Compact 6-3-2. The high outlier is Particle AGR1-632-60.	18
Figure 15. Normalized Ru-103/Cs-137 activity ratio for 60 particles from irradiated Compact 6-3-2. The high outliers are Particle AGR1-632-60 and Particle AGR1-632-52.	18
Figure 16. Normalized Sb-125/Cs-137 activity ratio for 60 particles from irradiated Compact 6-3-2.	19
Figure 17. Typical cross sections of burned-back, irradiated fuel particles from Compact 6-3-2 after grinding and polishing Mount 21T.	22
Figure 18. Stringers of buffer material across back-potted epoxy to IPyC layer.	23
Figure 19. Radial buffer cracks, one of which evidently induced an IPyC fracture on left side.	24
Figure 20. Kernel protrusion into buffer fractures.	24
Figure 21. Wide buffer fractures without large kernel pores.	25
Figure 22. Preparation damage in Mount 22T, with kernel and buffer dislodged from left particle.	26
Figure 23. Type Bi morphology found in four Mount 22T particles.	26
Figure 24. Typical fractured buffer particle in Mount 22T.	27
Figure 25. Silicon carbide remnant from Particle AGR1-632-30 in Mount 47T.	28
Figure 26. Particles AGR1-632-34 (left) and AGR1-632-39 (right) within Mount 48T.	29
Figure 27. Mount 48T Particle AGR1-632-35, where the buffer remained bonded to the IPyC layer.	29
Figure 28. Distribution of particle types found in Compact 6-3-2 Mounts 21T, 22T, and 48T.	30

Figure 29. Distribution of particle types among compacts from AGR-1 Capsule 6.	30
Figure A-1. Deconsolidation configuration.	38
Figure A-2. Framework with deconsolidation tube/vial (left) and two Soxhlet extractor stations.	39
Figure B-1. Cutaway view of camera optical orientation without shielding	43
Figure B-2. Assembled isometric view of microscope stages and shielding.....	43
Figure B-3. Post deconsolidation particle viewed on the end of the vacuum tweezer needle.	44
Figure B-4. MFC Analytical Laboratory Cell 4 spectrometer configuration.....	44
Figure D-1. Particle morphologies observed in AGR-1 fuel particle cross sections, where “i” denotes an intact buffer and “f” denotes a fractured buffer.....	51

TABLES

Table 1. Identification and irradiation conditions for AGR-1 Compact 6-3-2.....	3
Table 2. Fission products in the deconsolidation and leach solutions from Compact 6-3-2 expressed as decay-corrected activity (Bq) and compact fraction (based on calculated inventories [Sterbentz 2011]).	7
Table 3. Uranium and plutonium inventory in the deconsolidation and leach solutions from Compact 6-3-2 expressed as total mass (μg) and compact fraction (based on calculated inventories [Sterbentz 2011]).	8
Table 4. Decay-corrected activities (in Bq) for isotopes measured by gamma counting of particles from irradiated Compact 6-3-2. Values in gray indicate decay-corrected activities calculated using the MDA for cases in which no activity was detected. ^a	11
Table 5. Average decay-corrected activities and average ratio of measured to calculated activities. Calculated activities per particle are based on ECAR-958 Rev. 1 and 4,145 particles per compact.....	13
Table 6. Measured and calculated burnup values for Compact 6-3-2.....	20

ACRONYMS

AGR	Advanced Gas Reactor
ATR	Advanced Test Reactor
DLBL	deconsolidation-leach-burn-leach
FIMA	fissions per initial metal atom
HFEF	Hot Fuel Examination Facility
ICP-MS	inductively coupled plasma mass spectroscopy
IMGA	irradiated microsphere gamma analysis
INL	Idaho National Laboratory
IPyC	inner pyrolytic carbon
MDA	minimum detectable activity
MFC	Materials and Fuel Complex
NGNP	Next Generation Nuclear Plant
OPyC	outer pyrolytic carbon
PIE	post-irradiation examination
TRISO	tristructural isotropic
VHTR	Very High Temperature Reactor

AGR-1 Fuel Compact 6-3-2 Post-Irradiation Examination Results

1. INTRODUCTION

1.1 Background

The Next Generation Nuclear Plant (NGNP) Fuel Development and Qualification Program was established to perform the requisite research and development on tristructural isotropic (TRISO) coated particle fuel to support deployment of a very high temperature reactor (VHTR). The overarching program goal is to provide a baseline fuel qualification data set to support licensing and operation of a VHTR. To achieve these goals, the program includes the elements of fuel fabrication, irradiation, post-irradiation examination (PIE) and safety testing, fuel performance, and fission product transport (Simonds 2010).

A series of fuel irradiation experiments is being planned and conducted in the Advanced Test Reactor (ATR) at Idaho National Laboratory (INL). These experiments will provide data on fuel performance under irradiation, support fuel process development, qualify the fuel for normal operating conditions, provide irradiated fuel for safety testing, and support the development of fuel performance and fission product transport models. The first of these Advanced Gas Reactor (AGR) irradiation tests, designated AGR-1, began in the ATR in December of 2006 and ended in November 2009. This experiment was conducted primarily to act as a shakedown test of the multicapsule test train design and provide early data on fuel performance for use in fuel fabrication process development. It also provided samples for post-irradiation safety testing, where fission product retention of the fuel at high temperatures will be experimentally measured. The capsule design and details of the AGR-1 experiment have been presented previously (Grover, Petti, and Maki 2010).

The AGR-1 fuel particles and compacts were fabricated at Oak Ridge National Laboratory using 350 μm diameter 19.7% enriched uranium oxide-uranium carbide (UCO) kernels produced by Babcock and Wilcox, Inc. The particles were pressed into right cylindrical compacts that are nominally 25 mm long and 12.4 mm in diameter and contain approximately 4,100 coated particles. The fuel compacts have ~ 1.5 mm thick fuel-free end caps at the top and bottom as shown in Figure 1. A baseline fuel type and three fuel variants were included in the AGR-1 irradiation, with each variant fabricated by varying one step of the coating process to produce slightly different inner pyrolytic carbon (IPyC) or SiC coating properties. A summary of particle and compact properties is presented in the AGR-1 Test Plan (Maki 2009). One key goal of the experiment is to identify any fuel performance differences between the fuel types, either during the irradiation or during post-irradiation high temperature safety tests, in order to support optimization of the fuel fabrication process and eventual selection of a reference fuel for qualification.

A total of 72 compacts were irradiated in the AGR-1 experiment. The experiment completed 620 effective full-power days in the reactor and achieved a peak calculated compact-average burnup of 19.5% fissions per initial metal atom (FIMA) with zero particle failures observed, based on the measured fission gas release-to-birth rate ratios (Grover 2010). At completion of the irradiation, the test train was shipped to the Materials and Fuels Complex (MFC) at the INL to initiate PIE and high temperature safety testing. The primary objectives of the AGR-1 PIE and safety testing are to: (a) assess the overall performance of the test train and components and provide data to verify the test train thermal analyses; (b) evaluate the fission product retention of the fuel during the irradiation and during high temperature post-irradiation safety tests; and (c) characterize the fuel compacts and individual particles to assess the condition of the matrix material, kernels, and coatings and document any concerns. Details of the activities planned as part of the PIE and safety testing, including the planned activities for specific compacts, have been described in the AGR-1 Post-Irradiation Examination Plan (Demkowicz 2010).

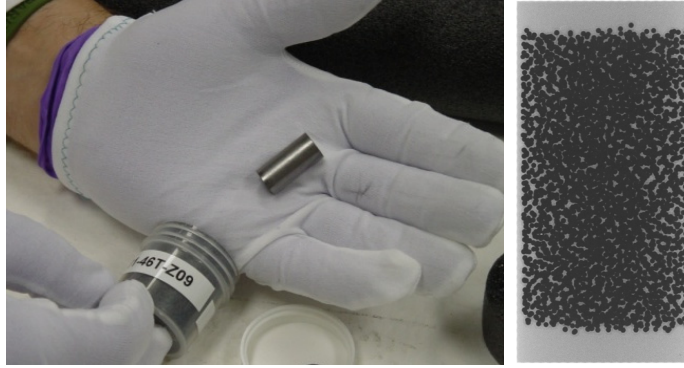


Figure 1. Photograph (left) and x-radiograph (right) of an unirradiated AGR-1 fuel compact. Uranium oxide-uranium carbide kernels and non-fueled end caps are clearly visible in the x-radiograph.

Upon receipt at MFC, the AGR-1 test train was unpackaged, visually inspected, and examined using gamma spectrometry. The test train was then sectioned into individual capsules that were opened to remove the fuel compacts and other internal capsule components for PIE. The fuel compacts, graphite fuel holders, and metal capsule shells were measured to determine the degree of dimensional change that occurred during the irradiation. Results of test train inspection and nondestructive examination, disassembly, and dimensional measurements are presented in the report, *AGR-1 Irradiated Test Train Preliminary Inspection and Disassembly First Look* (Demkowicz et al. 2011). All of the irradiated AGR-1 fuel compacts were also gamma scanned in axial increments to determine the inventory of fission products and experimentally measure the burnup prior to proceeding with destructive PIE (Harp 2011).

1.2 Compact 6-3-2 PIE objectives and overview

Compact 6-3-2 is composed of Baseline fuel particles and was located in Stack 2, Level 3 of Capsule 6 in the AGR-1 irradiation experiment (Maki 2009). Details of the fuel particle and compact fabrication and properties are presented in the AGR-1 Baseline particle (Hunn and Lowden 2006) and compact (Hunn, Montgomery, and Pappano 2006) data packages. Some of the important irradiation conditions for Compact 6-3-2 are listed in Table 1. The specific PIE objectives for Compact 6-3-2 are to:

1. Perform deconsolidation-leach-burn-leach (DLBL) analysis to (a) identify the number of particles in the compact with a defective SiC coating, (b) determine the inventory of fission products outside of the SiC layer, and (c) provide particles for subsequent examination.
2. Perform gamma-ray spectrometry on a subset of particles to quantify the inventory of major fission products in order to examine variations in fission product retention.
3. Perform mass spectrometric burnup analysis on a subset of particles for comparison with AGR-1 physics predictions and gamma spectrometric measurements.
4. Examine kernel and coating microstructures of selected particles in order to better understand fuel irradiation behavior and mechanisms of fission product diffusion and release. Examination methods include optical microscopy, electron microscopy (scanning electron microscopy, transmission electron microscopy), and elemental analysis (energy dispersive spectroscopy, wavelength dispersive spectroscopy).

Because Compact 6-3-2 was the first fuel compact to undergo PIE at INL as part of the NGNP Fuels program, it is also intended that this compact serve as a shakedown for all of the TRISO fuel PIE methods and equipment at INL. A flow chart of the analysis completed on Compact 6-3-2 is provided in Figure 2. The results of dimensional measurements and gamma scanning have been presented in separate reports (Demkowicz et al. 2011, Harp 2011).

Table 1. Identification and irradiation conditions for AGR-1 Compact 6-3-2.

Compact ID ^a	Fabrication ID	Fuel type	Burnup (% FIMA ^{b,c})	Fast Fluence $\times 10^{25}$ (n/m ²) ^c	Irradiation Temperature (°C) ^d
AGR-1 6-3-2	LEU01-46T-Z69	Baseline	11.31	2.38	1070

a. The X-Y-Z naming convention denotes the location in the irradiation test train: Capsule-Level-Stack.
b. Fissions per initial metal atom.
c. Based on physics calculations (Sterbentz 2011)
d. Volume averaged time averaged temperature, based on thermal calculations (Hawkes 2012)

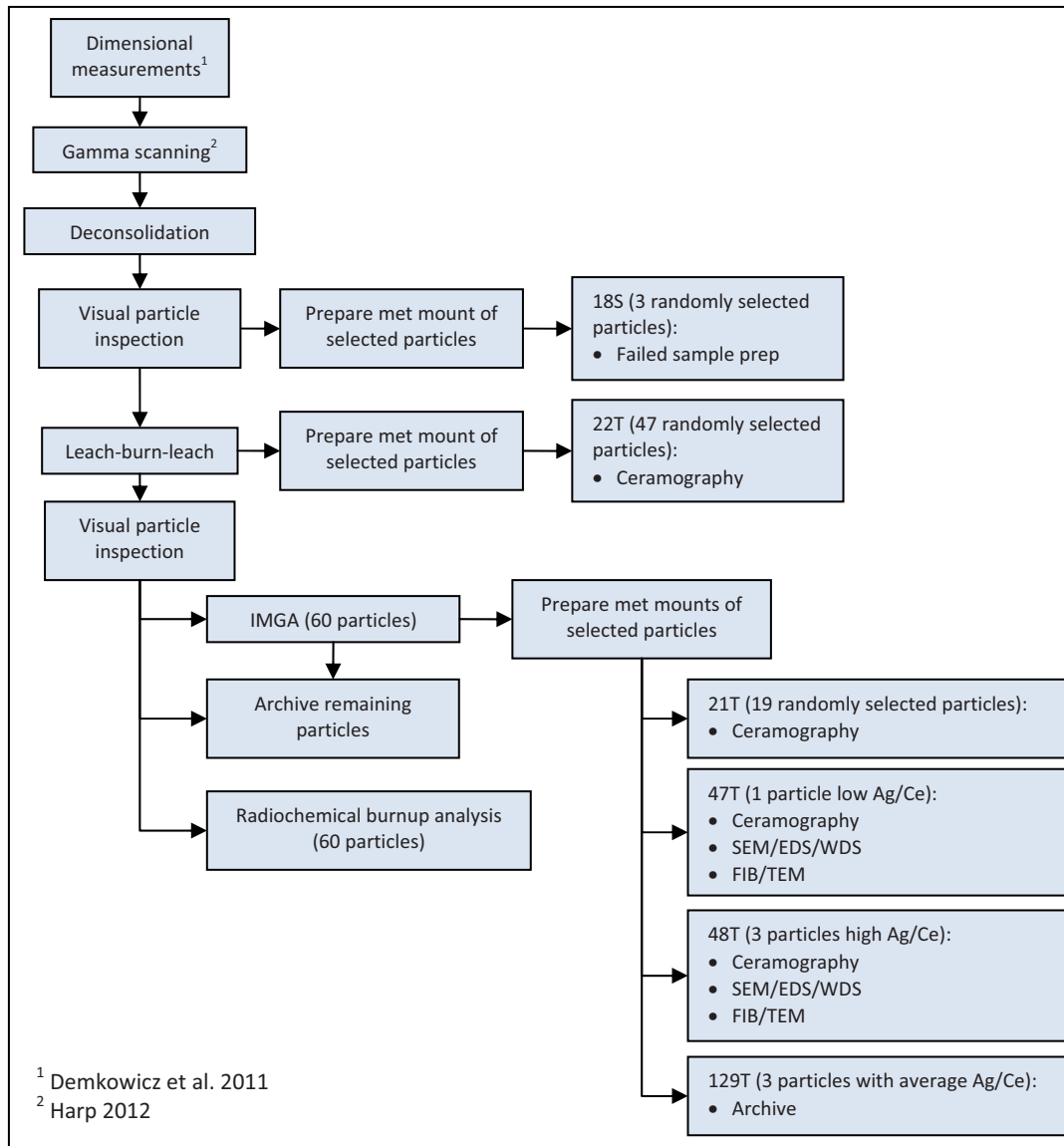


Figure 2. PIE flow chart for Compact 6-3-2.

2. DECONSOLIDATION-LEACH-BURN-LEACH

The general process for compact deconsolidation and leach-burn-leach analysis is given in Appendix A. Compact 6-3-2 was received in the Analytical Laboratory on September 15, 2010. Receipt weight was 5.4680 g. The entire DLBL process was performed in Hot Cell 5 in the Analytical Laboratory A-wing. Deconsolidation was performed on September 17, 2010. During deconsolidation, current was maintained between 0.9 and 1 amp, and voltage varied from 8.3 V initially to 7.1 V at the end of the step. Deconsolidation took 69 minutes and the average power input was 7.73 watts. The process began with some dark turbidity below the compact resulting from the generation of graphite fines. Particles began to drop through the perforated support and continued to do so for the next 50 minutes, at which time the breakdown was recorded as 90% complete. Between 60 and 69 minutes, hydrogen bubbles continued to be emitted from the electrode wires, until the anode appeared to be resting on the perforated support. Following removal of the anode foot from the deconsolidation tube, three approximately 5-mm diameter pieces remained. These were flushed into the thimble prior to transfer to the Soxhlet extractor. Figures 3–5 show some photographs taken during various stages of deconsolidation.

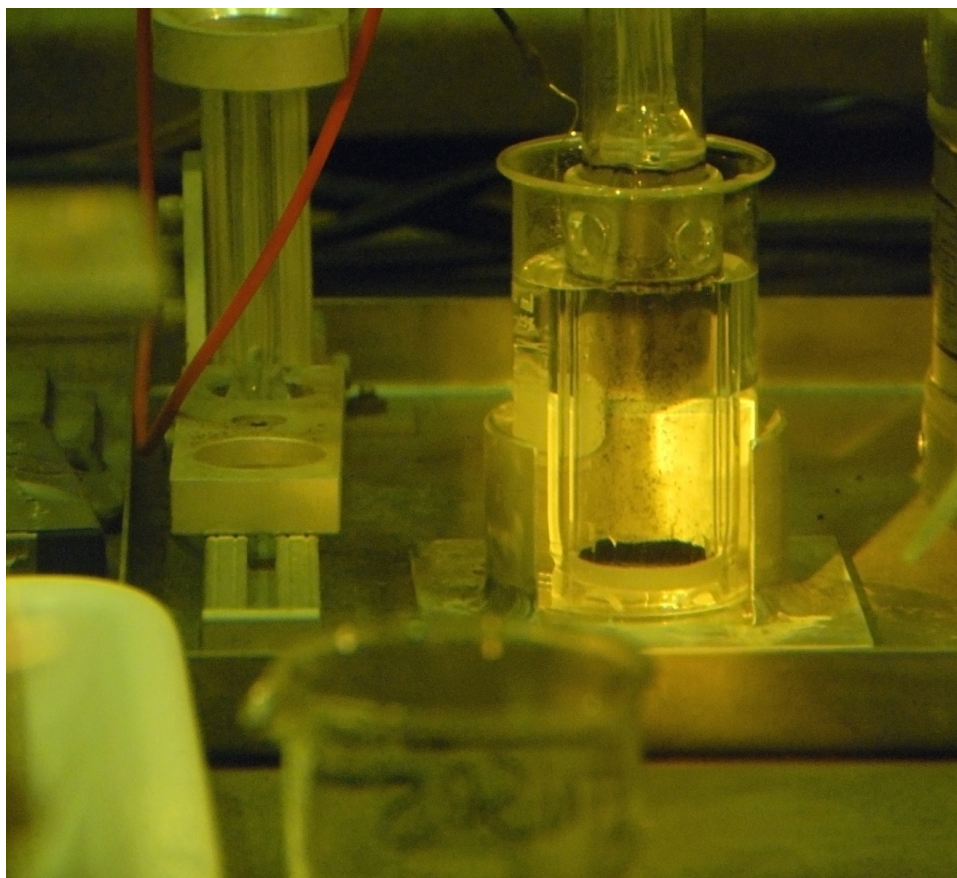


Figure 3. Deconsolidation in Cell 5 showing particles dropping down from compact and accumulating on thimble frit.

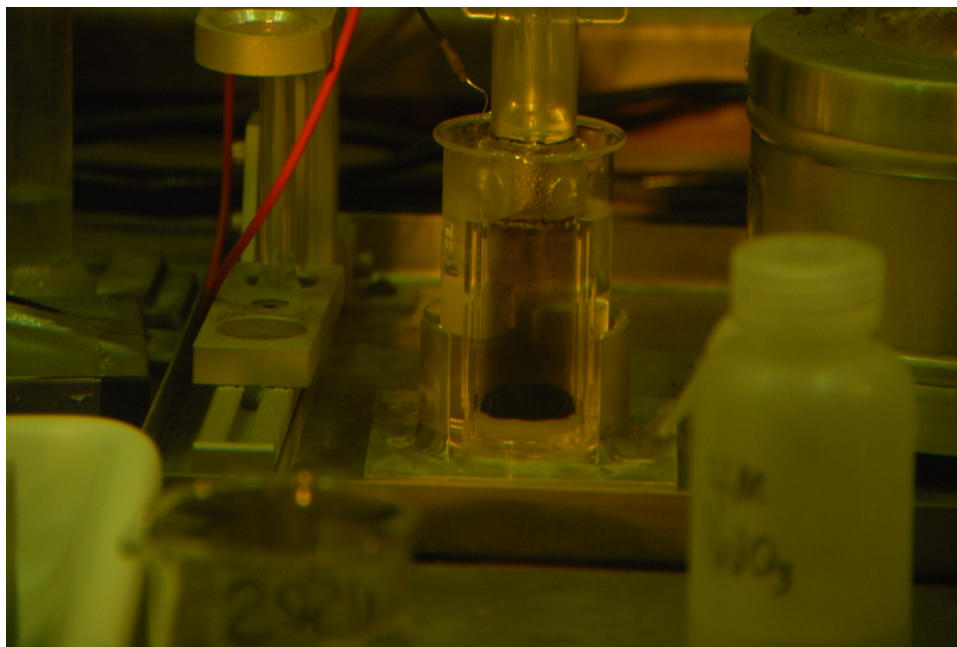


Figure 4. Increased turbidity toward the end of deconsolidation.

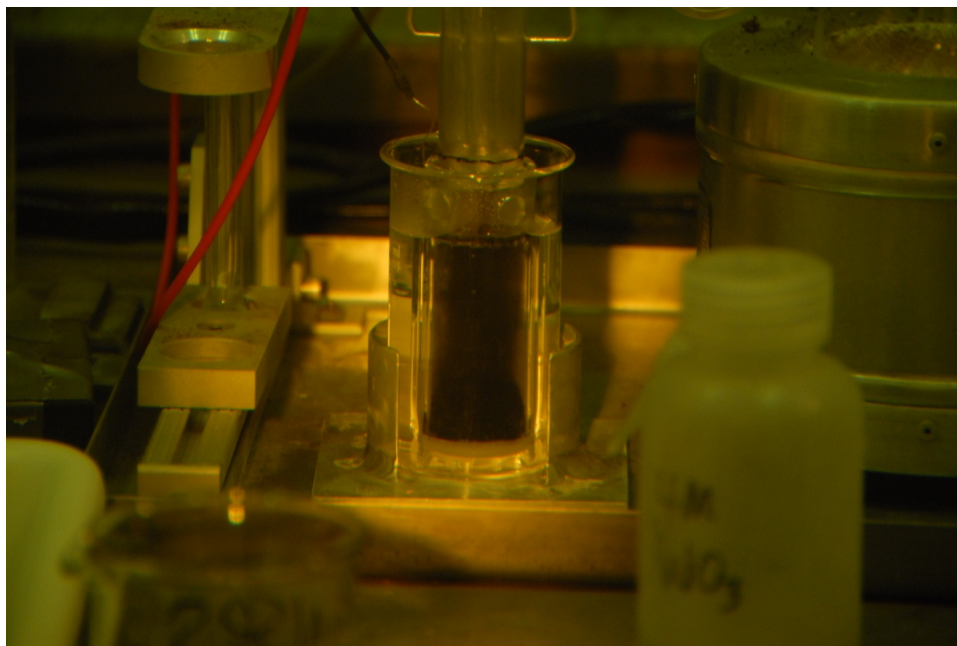


Figure 5. Highly turbid solution at end of deconsolidation.

The first two 24-hour pre-burn leaches were performed between September 20 and 23, 2010. The period for the siphon cycle during the first leach was approximately 6.5 minutes. The thimble appeared to drain approximately 25% during the 30 seconds in which the siphon drains the collection volume. Incomplete draining occurred because fines plugged the voids in the frit at the bottom of the thimble. The siphon cycle time for the second pre-burn leach was 6 minutes. The first extraction ran 24 hours, and the second took 23 hours 50 minutes. Some flexibility is allowed in initiating and completing steps so that the succeeding step can be initiated to proceed unattended before the end of a work day.

Following the second pre-burn leach step, the thimble was transferred to a covered fused-silica beaker, which was put into the Vulcan muffle furnace. The operating temperature of 750°C was reached at 10:45 a.m. on September 23, and the burn step was terminated on September 26, 2010. Air cooling flow was maintained at a rate that caused the pinwheel mounted above the exhaust chimney to barely rotate. This was done to assure that a minimum oxygen flow was maintained.

The post-burn leaches were started on September 27 and completed on September 30. The first leach duration was 23 hours 50 minutes, and the second was 24 hours. Siphon cycle times for these leaches were 18 minutes and 17 minutes, respectively. The increased cycle times reflect the more complete draining of the siphon volume because the fine carbon that restricted draining of the thimble in the first two leaches was oxidized during the burn step. The thimble appeared to retain only 10% of its volume during siphon cycles.

The net weight of particles in the thimble following the entire deconsolidation leach-burn-leach cycle was 2.3465 g. Grab samples of particles were taken following deconsolidation, after the pre-burn leach cycles, and after the post-burn leaches. The masses of these particles were 0.2730 g post-deconsolidation, 0.0739 g following pre-burn leaches, and 0.1180 g following post-burn leaches. The grab samples were taken using a miniature scoop attached to a manipulator-adapted handle.

The deconsolidation solution and the pre-burn and post-burn leach solutions were analyzed using gamma spectrometry and mass spectrometry. 10 mL aliquots of all of the deconsolidation and leach solutions were taken from the nominal 150 to 200 mL leach volumes. The samples were transferred to the B-wing counting rooms of the Analytical Laboratory in MFC-752 to facilitate gamma spectrometry with less background interference than would be observed in the A-wing Hot Cell 4 spectrometer. In the B-wing the solutions were counted on Detector B. Detector B, located in lab B-30, is a +3000 V HPGE coaxial detector connected to a Canberra digital MCA and uses APEX peak analysis software. The detector resides within a steel vault that has walls approximately 10" thick to provide shielding. This detector is very flexible with respect to the counting geometries and calibrated for use with a maximum sample-to-detector distance of 1 meter. Samples are placed on plastic jigs that allow precise placement in relation to the detector. Samples are placed in a jig to ensure repeatable geometry between calibration and various samples. A multiline gamma source ranging from 59.4 to 1,836 keV was used to calibrate the detector.

To measure Sr-90 inventory, strontium was separated onto a solid crown-ether ion exchange medium, then eluted from the media, and precipitated as a carbonate. A Tennelec gas-flow proportional unit was used to determine the amount of beta activity per mass of precipitate to determine sample Sr-90 content. Mass spectrometric analysis of the DLBL solutions was performed using a VG Plasma Quad Inductively-Coupled Plasma Mass Spectrometer.

The inventory of selected fission products in each of the five DLBL solutions is given in Table 2, both as decay-corrected activity (all activity values presented in this report have been decay-corrected to 11/7/2009 12:00 GMT, the end of the AGR-1 irradiation plus 1 day) and the equivalent Compact 6-3-2 fraction, based on the predicted compact inventories provided in ECAR-958, Rev. 1 (Sterbentz 2011). All of the decay corrections discussed in this report were calculated using the equation

$$A = A_0 e^{-\lambda t} \quad (1)$$

where A is the activity at time t , A_0 is the activity at $t = 0$, and λ is the decay constant ($\lambda = \ln(2)/t_{1/2}$, and $t_{1/2}$ is the half life). Isotope half life data were taken from the ENDF/B-VII.1 library (Chadwick et al. 2011). The inventory of uranium and plutonium isotopes in the solutions is given in Table 3 in absolute measured mass and equivalent compact fraction (no decay correction has been applied to the U and Pu data). Note that in these tables, a compact fraction of 2.4×10^{-4} is equivalent to a single particle inventory (based on 4,145 particles per compact). In cases where the activity or mass was below the detection limit

for the method, the minimum detectable activity (MDA) was used to calculate the values in the tables and these values were included in the process totals. If the entries based on MDAs accounted for >50% of the total, then the total was listed as a threshold value (preceded by “<”).

The data in Table 3 indicate that the approximate uranium equivalent of a single kernel was dissolved in the first post-burn leach solution, suggesting a single particle with a defective SiC layer. Previous evidence for this was found in the Capsule 6 graphite holder, which showed slightly elevated Cs-134 activity in the graphite holder at the location that had been occupied by Compact 6-3-2 during irradiation (increased cesium release is an expected behavior for a particle with defective SiC layer) (Harp and Ploger 2011). In addition, the total decay-corrected Cs-134 activity found in the Capsule 6 components (including the graphite holder, capsule shell, and graphite spacers) was 1.8×10^6 Bq (Harp, Demkowicz, and Ploger 2012), which is equivalent to approximately 98% of the inventory of an average Compact 6-3-2 particle. These results indicate that the method used to gamma scan the graphite holders in the Hot Fuels Examination Facility (HFEF) was capable of detecting the released cesium from a single defective particle.

As indicated in Table 2, the inventory of most of the isotopes analyzed (Ce-144, Cs-134, Cs-137, Ru-106, Sb-125, Zr-95) was very low. The majority of the activity came from the first post-burn leach in which a whole fuel kernel was presumably dissolved. Eliminating the post-burn leach solutions from the totals, the inventory of these isotopes was below a compact fraction of 1×10^{-5} .

Table 2. Fission products in the deconsolidation and leach solutions from Compact 6-3-2 expressed as decay-corrected activity (Bq) and compact fraction (based on calculated inventories [Sterbentz 2011]).

	Activity (Bq) ^a									
	Ag-110m	Ce-144	Cs-134	Cs-137	Eu-154	Eu-155	Ru-106	Sb-125	Sr-90	Zr-95
Deconsolidation	4.69E+3	1.5E+5	7.10E+3	1.82E+4	9.03E+5	6.54E+5	<2E+4	<4E+3	1.49E+6	2.2E+5
1 st Pre-burn leach	<8E+2	9.9E+4	7.00E+3	1.41E+4	1.73E+5	1.27E+5	1.4E+4	<1E+3	4.74E+5	5.E+04
2 nd Pre-burn leach	<9E+1	6.2E+3	1.42E+3	4.27E+3	4.34E+3	2.87E+3	<7E+2	<1E+2	2.31E+4	<3E+3
1 st Post-burn leach	7.E+3	2.87E+7	5.7E+5	1.23E+6	6.6E+5	3.1E+5	<3E+4	1.1E+5	2.45E+6	7.5E+6
2 nd Post-burn leach	<2E+2	1.66E+4	9.53E+2	3.06E+3	8.56E+3	5.74E+3	<7E+2	1.96E+3	4.20E+3	1.0E+4
	Compact fraction ^b									
	Ag-110m	Ce-144	Cs-134	Cs-137	Eu-154	Eu-155	Ru-106	Sb-125	Sr-90	Zr-95
Deconsolidation	7.72E-5	8.6E-7	9.07E-7	1.59E-6	3.14E-3	2.80E-3	<7E-7	<5E-6	9.18E-5	8.4E-7
1 st Pre-burn leach	<1E-5	5.8E-7	8.94E-7	1.23E-6	6.04E-4	5.46E-4	4.8E-7	<2E-6	2.91E-5	2.E-07
2 nd Pre-burn leach	<2E-6	3.6E-8	1.81E-7	3.72E-7	1.51E-5	1.23E-5	<2E-8	<2E-7	1.42E-6	<1E-8
1 st Post-burn leach	1.E-04	1.68E-4	7.2E-5	1.07E-4	2.3E-3	1.3E-3	<1E-6	1.3E-4	1.50E-4	2.9E-5
2 nd Post-burn leach	<3E-6	9.71E-8	1.22E-7	2.67E-7	2.98E-5	2.46E-5	<2E-8	2.42E-6	2.58E-7	4.0E-8
Process Totals	2.2E-04	1.7E-04	7.4E-05	1.1E-04	6.1E-03	4.7E-03	<2E-06	1.4E-04	2.7E-04	3.0E-05
a. Measured activity data taken from AL Report #92984 (2011).										
b. Note that a fraction of 2.4E-4 is equivalent to a single particle inventory.										

Table 3. Uranium and plutonium inventory in the deconsolidation and leach solutions from Compact 6-3-2 expressed as total mass (μg) and compact fraction (based on calculated inventories [Sterbentz 2011]).

	Mass (μg) ^a					
	U-234	U-235	U-236	U-238	Pu-239	Pu-240
Deconsolidation	<4E-3	1.00E-1	<5E-3	1.65E+0	8.7E-2	1.5E-2
1st Pre-burn leach	<2E-2	3.1E-2	<2E-2	3.42E-1	<6E-2	<5E-2
2nd Pre-burn leach	<9E-2	<9E-2	<1E-1	5.24E-1	<3E-1	<3E-1
1st Post-burn leach	6.15E-1	2.06E+1	5.24E+0	1.95E+2	2.43E+0	1.29E+0
2nd Post-burn leach	<2E-2	<2E-1	<2E-1	1.29E-1	<8E-2	<7E-2
	Compact fraction ^b					
	U-234	U-235	U-236	U-238	Pu-239	Pu-240
Deconsolidation	<1E-3	1.3E-6	<3E-7	2.3E-6	9.6E-6	4.3E-6
1st Pre-burn leach	<7E-3	4.1E-7	<1E-6	4.8E-7	<7E-6	<1E-5
2nd Pre-burn leach	<3E-2	<1E-6	<6E-6	7.3E-7	<3E-5	<9E-5
1st Post-burn leach	2.2E-1	2.7E-4	3.0E-4	2.7E-4	2.7E-04	3.7E-4
2nd Post-burn leach	<7E-3	<3E-6	<1E-5	1.8E-7	<9E-6	<2E-5
Process totals	2.7E-1	2.8E-4	3.2E-4	2.8E-4	3.3E-4	4.9E-4

a. Measured mass data taken from AL Report #92984 (2011).

b. Note that a fraction of 2.4E-4 is equivalent to a single particle inventory.

Several isotopes exhibited elevated levels in the solutions and deserve further discussion. The total fraction of the compact Ag-110m inventory in the pre-burn solutions was about 9.2×10^{-5} (equivalent to 0.4 particles). It is not clear if this relatively small amount of silver was released primarily from the single particle with defective SiC, or if it was released through intact coatings of all particles. This amount of Ag-110m is relatively small compared to the amount of Ag-110m found in the Capsule 6 components (data indicate that ~38% of the total Capsule 6 Ag-110m inventory was found on the capsule components [Harp, Demkowicz, and Ploger 2012]).

The total fraction of the compact Eu-154 and Eu-155 inventory in the solutions was 6.1×10^{-3} and 4.7×10^{-3} respectively (equivalent to the inventory of 25 and 20 particles respectively). The total fraction of Sr-90 in the solutions was 2.7×10^{-4} , roughly equivalent to the predicted inventory in a single particle, with about 0.6 particles in the post-burn leach solutions (associated with the single leached kernel) and another 0.5 particles in the deconsolidation and pre-burn leach solutions.

The europium release data are clearly indicative of release from intact fuel particles, since the inventory is far in excess of the single kernel leached in the post-burn leaches. Because the Ag-110m and Sr-90 data indicate total releases of ~1 particle equivalent inventory when summing results from all solutions, it is not clear whether this reflects diffusive release from intact fuel or release from the single particle with a defective SiC layer.

3. PARTICLE INSPECTION AND IRRADIATED MICROSPHERE GAMMA ANALYSIS

3.1 Visual inspection

Details of the equipment and procedures for visual particle inspection and gamma spectrometry of individual particles are given in Appendix B. Following deconsolidation, a sample of the fuel particles from Compact 6-3-2 was taken by removing a small quantity of material from the thimble as shown in Figure 6. A quantity of separated compact matrix remained, seen as flakes and chunks of material with concavities from particles that were released in the electrolytic deconsolidation process. The sample taken following deconsolidation weighed 0.0273 g. From the baseline value of 7.27×10^{-4} g/particle (Maki 2009), and disregarding the mass of any matrix debris, this sample consisted of approximately 40 particles. All particles were essentially spheroidal and consistent in color, being uniformly gray in appearance. No examples of loss of outer pyrolytic carbon (OPyC) were noted.

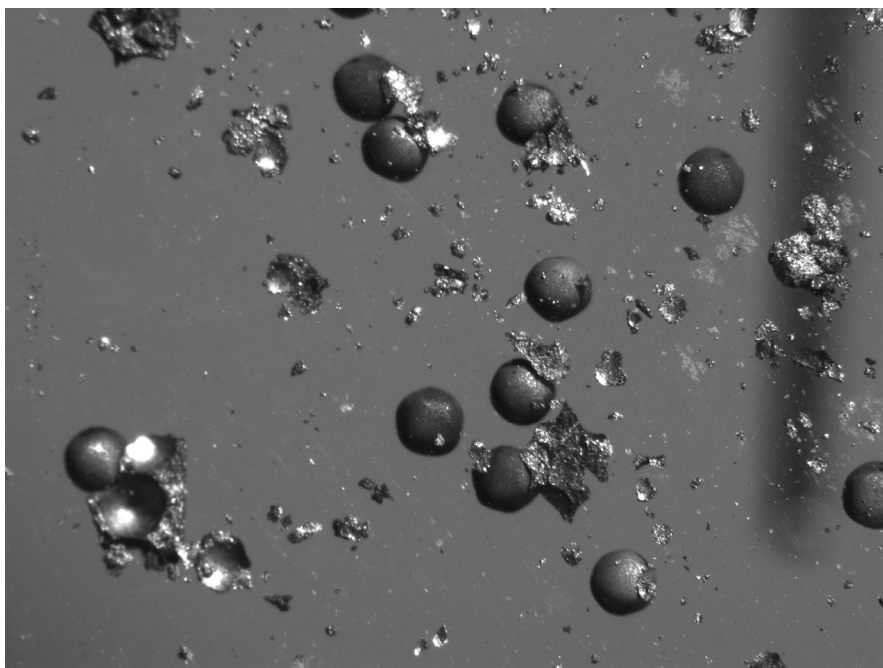


Figure 6. Deconsolidated particles and residual matrix debris from Compact 6-3-2.

Based on the uranium data from the deconsolidation-leach-burn-leach analysis, there was apparently one particle with a defective SiC layer (see discussion in Section 2). A visual examination of the particles was undertaken to identify this particle and preserve it for further detailed analysis. Following completion of the second post-burn leach, all of the particles were sequentially transferred to the inspection dish in several stages and inspected. No definitive evidence of this particle (either an intact particle with different appearance because of the empty SiC shell or pieces of a broken SiC shell) was found. It is possible that following the burn-leach step the remaining broken SiC shell fractured into multiple pieces that were subsequently lost.

Inspection of particles following the second post-burn leach revealed SiC surfaces that were generally uniform in coloration with a slightly more reflective and slightly less granular appearance when compared to particles after deconsolidation as shown in Figure 7. Some particles had irregular dark markings on the SiC surface (see Figures 7 (b–e)) but no obvious evidence of cracks or other mechanical damage in the SiC was observed. Some of the particles exhibited conspicuous concave depressions (see Figure 7(e)).

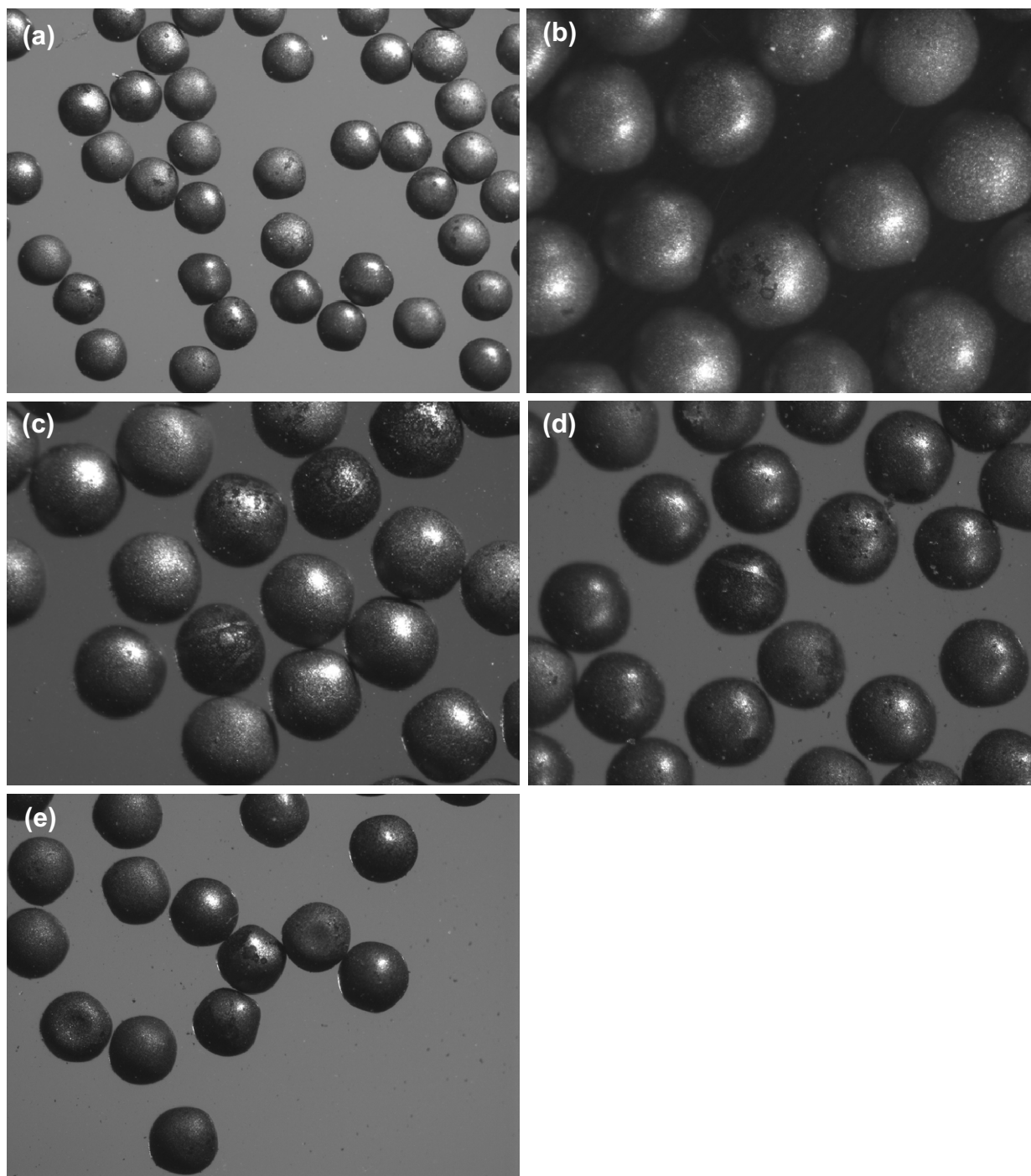


Figure 7. Representative photographs of Compact 6-3-2 particles during visual inspection following the second post-burn leach.

3.2 Irradiated microsphere gamma analysis

Sixty particles from Compact 6-3-2 were gamma counted following the second post-burn leach. Individual particles were selected using the inspection system described in Appendix B. As this compact represented a shakedown of experimental methods, a variety of counting times were used, between 20 minutes and 84 hours live time (the latter representing a counting duration that extended over a long

weekend). It was found that longer count times (> 2 hours) were required to reliably quantify the Ag-110m inventory for particles from this fuel compact. Details of the gamma counting equipment and procedure are given in Appendix B.

Table 4 gives the decay-corrected activity of each isotope measured in the particles. In several cases, no Ag-110m or Eu-155 activity was detected and the MDA was used to calculate the decay-corrected activities in the table instead (values in gray text and preceded by “<”). Table 5 provides the average activity of the analyzed particles in Bq as well as the average ratio of measured-to-calculated activity. The measured-to-calculated activity ratio was determined using the compact activities listed in ECAR-958 (Sterbentz 2011) and using a value of 4,145 particles per compact for the AGR-1 Baseline compacts (Hunn, Montgomery, and Pappano 2006). The ratio is calculated for each isotope, X , using the equation

$$\frac{\overline{A^X}}{A_{632(calc)}^X/4145} \quad (2)$$

where:

$\overline{A^X}$ = is the average measured activity of isotope X for all n particles measured ($\overline{A^X} = \sum_{i=1}^n \left(\frac{1}{n}\right) A_i^X$),
and $A_{632(calc)}^X$ is the calculated activity of isotope X for Compact 6-3-2.

Table 4. Decay-corrected activities (in Bq) for isotopes measured by gamma counting of particles from irradiated Compact 6-3-2. Values in gray indicate decay-corrected activities calculated using the MDA for cases in which no activity was detected.^a

Particle #	Ag-110m	Ce-144	Cs-134	Cs-137	Eu-154	Eu-155	Ru-103	Ru-106	Sb-125	Zr-95
AGR1-632-11	<1E+4	3.52E+7	1.56E+6	2.45E+6	5.38E+4	3.86E+4	3.61E+7	5.11E+6	1.38E+5	5.71E+7
AGR1-632-12	1.02E+4	3.46E+7	1.46E+6	2.31E+6	5.82E+4	<4E+4	3.61E+7	5.19E+6	1.24E+5	5.73E+7
AGR1-632-13	<1E+4	3.42E+7	1.56E+6	2.38E+6	4.77E+4	<3E+4	3.37E+7	5.44E+6	1.14E+5	5.55E+7
AGR1-632-14	<1E+4	3.26E+7	1.40E+6	2.25E+6	4.85E+4	<4E+4	3.13E+7	4.82E+6	1.19E+5	5.43E+7
AGR1-632-15	<1E+4	3.62E+7	1.58E+6	2.54E+6	5.26E+4	<3E+4	3.61E+7	5.72E+6	1.14E+5	5.92E+7
AGR1-632-16	9.21E+3	3.69E+7	1.52E+6	2.42E+6	5.22E+4	<3E+4	3.85E+7	5.96E+6	1.38E+5	6.06E+7
AGR1-632-17	1.03E+4	3.66E+7	1.43E+6	2.39E+6	5.02E+4	<4E+4	4.17E+7	5.68E+6	1.52E+5	6.38E+7
AGR1-632-18	<9E+3	3.15E+7	1.27E+6	2.12E+6	4.57E+4	<3E+4	3.92E+7	5.26E+6	1.05E+5	5.43E+7
AGR1-632-19	1.03E+4	3.53E+7	1.43E+6	2.33E+6	4.58E+4	<2E+4	3.99E+7	5.67E+6	1.14E+5	6.05E+7
AGR1-632-21	<6E+3	3.61E+7	1.57E+6	2.41E+6	5.34E+4	2.53E+4	3.74E+7	5.18E+6	1.19E+5	5.81E+7
AGR1-632-22	<4E+3	3.93E+7	1.58E+6	2.59E+6	5.30E+4	2.31E+4	4.24E+7	6.42E+6	1.24E+5	6.77E+7
AGR1-632-23	<4E+3	3.56E+7	1.53E+6	2.42E+6	5.34E+4	<2E+4	3.55E+7	5.19E+6	1.24E+5	5.61E+7
AGR1-632-24	<6E+3	3.72E+7	1.58E+6	2.47E+6	5.58E+4	2.14E+4	3.81E+7	5.48E+6	1.19E+5	6.22E+7
AGR1-632-25	1.03E+4	3.91E+7	1.69E+6	2.71E+6	5.54E+4	2.96E+4	4.32E+7	5.89E+6	1.29E+5	6.38E+7
AGR1-632-26	<7E+3	3.26E+7	1.38E+6	2.19E+6	4.22E+4	<2E+4	3.55E+7	5.16E+6	9.31E+4	5.69E+7
AGR1-632-27	1.24E+4	3.59E+7	1.50E+6	2.42E+6	5.10E+4	1.89E+4	4.32E+7	5.23E+6	1.19E+5	5.86E+7
AGR1-632-28	1.04E+4	4.35E+7	1.78E+6	2.86E+6	5.78E+4	<3E+4	5.09E+7	6.90E+6	1.39E+5	7.58E+7
AGR1-632-29	6.25E+3	3.88E+7	1.63E+6	2.63E+6	5.42E+4	2.28E+4	4.01E+7	5.61E+6	1.29E+5	6.36E+7
AGR1-632-30	3.03E+3	3.91E+7	1.50E+6	2.53E+6	5.16E+4	2.98E+4	5.18E+7	5.90E+6	1.30E+5	6.72E+7
AGR1-632-31	7.60E+3	4.11E+7	1.76E+6	2.83E+6	5.97E+4	3.07E+4	3.84E+7	6.17E+6	1.40E+5	6.62E+7
AGR1-632-32	<7E+3	3.96E+7	1.60E+6	2.59E+6	5.32E+4	4.75E+4	4.53E+7	5.87E+6	1.26E+5	6.77E+7
AGR1-632-33	8.47E+3	3.67E+7	1.53E+6	2.46E+6	5.08E+4	<2E+4	3.49E+7	5.14E+6	1.04E+5	5.88E+7
AGR1-632-34	1.01E+4	3.93E+7	1.71E+6	2.69E+6	5.68E+4	2.55E+4	3.84E+7	5.92E+6	1.37E+5	6.23E+7
AGR1-632-35	1.05E+4	3.53E+7	1.38E+6	2.31E+6	4.84E+4	1.73E+4	4.19E+7	5.44E+6	1.16E+5	6.13E+7
AGR1-632-36	6.29E+3	3.82E+7	1.65E+6	2.59E+6	5.48E+4	4.03E+4	4.50E+7	5.44E+6	1.29E+5	6.03E+7
AGR1-632-37	7.18E+3	4.16E+7	1.75E+6	2.76E+6	5.93E+4	<3E+4	4.26E+7	6.42E+6	1.40E+5	6.62E+7
AGR1-632-38	<5E+3	3.46E+7	1.49E+6	2.34E+6	5.00E+4	2.12E+4	3.20E+7	4.96E+6	1.06E+5	5.67E+7
AGR1-632-39	9.60E+3	3.81E+7	1.67E+6	2.68E+6	5.65E+4	2.55E+4	4.34E+7	5.87E+6	1.40E+5	6.16E+7
AGR1-632-40	<7E+3	3.77E+7	1.63E+6	2.59E+6	5.48E+4	2.29E+4	3.98E+7	5.57E+6	1.16E+5	6.14E+7

Particle #	Ag-110m	Ce-144	Cs-134	Cs-137	Eu-154	Eu-155	Ru-103	Ru-106	Sb-125	Zr-95
AGR1-632-41	<7E+3	3.60E+7	1.56E+6	2.45E+6	5.32E+4	2.59E+4	3.54E+7	5.44E+6	1.11E+5	5.89E+7
AGR1-632-42	<7E+3	4.07E+7	1.77E+6	2.76E+6	5.85E+4	2.72E+4	4.34E+7	5.93E+6	1.35E+5	6.44E+7
AGR1-632-43	6.55E+3	4.05E+7	1.75E+6	2.80E+6	5.93E+4	2.42E+4	3.98E+7	6.22E+6	1.43E+5	6.52E+7
AGR1-632-44	6.55E+3	4.04E+7	1.75E+6	2.76E+6	5.81E+4	2.55E+4	4.34E+7	5.99E+6	1.49E+5	6.42E+7
AGR1-632-45	1.02E+4	3.53E+7	1.40E+6	2.34E+6	4.64E+4	2.25E+4	3.88E+7	5.31E+6	1.20E+5	6.10E+7
AGR1-632-46	<4E+3	3.74E+7	1.65E+6	2.55E+6	5.65E+4	1.73E+4	3.84E+7	5.54E+6	1.24E+5	5.83E+7
AGR1-632-47	1.04E+4	3.90E+7	1.58E+6	2.57E+6	5.21E+4	2.81E+4	4.65E+7	6.08E+6	1.34E+5	6.70E+7
AGR1-632-48	5.90E+3	3.42E+7	1.44E+6	2.36E+6	4.81E+4	1.95E+4	3.68E+7	4.96E+6	1.23E+5	5.67E+7
AGR1-632-49	1.00E+4	4.37E+7	1.73E+6	2.86E+6	5.69E+4	1.86E+4	4.91E+7	6.43E+6	1.39E+5	7.41E+7
AGR1-632-50	<3E+3	3.67E+7	1.51E+6	2.47E+6	5.17E+4	2.04E+4	4.50E+7	5.41E+6	1.20E+5	6.00E+7
AGR1-632-51	2.23E+3	3.64E+7	1.54E+6	2.42E+6	5.13E+4	4.14E+4	4.17E+7	5.66E+6	1.22E+5	6.03E+7
AGR1-632-52	2.81E+3	3.18E+7	1.24E+6	2.09E+6	4.04E+4	2.34E+4	4.74E+7	4.81E+6	1.03E+5	5.38E+7
AGR1-632-53	<6E+3	3.71E+7	1.57E+6	2.54E+6	5.17E+4	2.78E+4	3.69E+7	5.33E+6	1.27E+5	6.12E+7
AGR1-632-54	8.10E+3	3.45E+7	1.37E+6	2.32E+6	4.65E+4	<1E+4	4.08E+7	5.31E+6	1.22E+5	5.78E+7
AGR1-632-55	6.81E+3	4.05E+7	1.72E+6	2.71E+6	5.58E+4	2.95E+4	4.78E+7	5.79E+6	1.32E+5	6.52E+7
AGR1-632-56	4.51E+3	4.06E+7	1.70E+6	2.77E+6	5.62E+4	2.26E+4	4.33E+7	5.69E+6	1.22E+5	6.53E+7
AGR1-632-57	9.36E+3	3.43E+7	1.33E+6	2.27E+6	4.41E+4	2.61E+4	4.21E+7	5.24E+6	1.04E+5	5.82E+7
AGR1-632-58	9.73E+3	3.80E+7	1.54E+6	2.51E+6	5.05E+4	2.65E+4	4.23E+7	6.07E+6	1.27E+5	6.55E+7
AGR1-632-59	<6E+3	3.90E+7	1.71E+6	2.73E+6	5.94E+4	<1E+4	3.96E+7	5.63E+6	1.28E+5	6.23E+7
AGR1-632-60	9.05E+3	4.38E+7	1.83E+6	2.95E+6	6.27E+4	2.39E+4	7.27E+7	1.10E+7	1.85E+5	7.44E+7
AGR1-632-61	9.05E+3	4.30E+7	1.70E+6	2.83E+6	5.46E+4	3.52E+4	5.55E+7	6.22E+6	1.41E+5	7.18E+7
AGR1-632-62	6.01E+3	3.68E+7	1.69E+6	2.57E+6	5.70E+4	2.70E+4	3.52E+7	6.13E+6	1.35E+5	5.80E+7
AGR1-632-63	5.79E+3	3.88E+7	1.65E+6	2.62E+6	5.54E+4	2.00E+4	4.21E+7	5.98E+6	1.21E+5	6.50E+7
AGR1-632-64	<3E+3	3.42E+7	1.45E+6	2.34E+6	4.77E+4	1.96E+4	3.70E+7	4.79E+6	1.17E+5	5.56E+7
AGR1-632-65	1.13E+3	3.77E+7	1.72E+6	2.61E+6	5.42E+4	4.06E+4	4.72E+7	5.49E+6	1.08E+5	5.91E+7
AGR1-632-66	8.26E+3	3.57E+7	1.43E+6	2.37E+6	4.82E+4	2.00E+4	3.77E+7	5.21E+6	1.21E+5	5.99E+7
AGR1-632-67	1.03E+4	3.61E+7	1.51E+6	2.45E+6	4.94E+4	<2E+4	3.63E+7	5.53E+6	1.23E+5	6.05E+7
AGR1-632-68	5.97E+3	3.45E+7	1.49E+6	2.41E+6	4.94E+4	2.00E+4	3.38E+7	5.28E+6	1.20E+5	5.56E+7
AGR1-632-69	9.41E+3	3.63E+7	1.45E+6	2.41E+6	4.78E+4	2.83E+4	4.96E+7	5.35E+6	1.16E+5	6.11E+7
AGR1-632-70	<5E+3	3.99E+7	1.84E+6	2.78E+6	5.99E+4	3.31E+4	3.79E+7	6.24E+6	1.26E+5	6.18E+7
AGR1-632-71	9.89E+3	3.99E+7	1.77E+6	2.74E+6	5.99E+4	2.87E+4	4.14E+7	6.30E+6	1.41E+5	6.49E+7
Average	7.45E+3	3.74E+7	1.58E+6	2.53E+6	5.28E+4	2.63E+4	4.13E+7	5.72E+6	1.26E+5	6.17E+7
SD	2.6E+3	2.9E+6	1.4E+5	2.0E+5	4.8E+3	7.8E+3	6.5E+6	8.3E+5	1.4E+4	4.9E+6

a. Measured activity data taken from AL Report #92984.

All of the measured-to-calculated ratios in Table 5 are below a value of 1.0. The primary potential causes for such a deviation would be (a) a bias in the calculated activity of the compact or (b) significant release of the isotopes from the particles during irradiation. Based on the inventory of fission products found in the Capsule 6 components (Harp, Demkowicz, and Ploger 2012) as well as the inventory found outside of the SiC layer based on the DLBL results (Table 2), it is clear that average release from the individual particles was usually significantly less than 1% with the exception of silver (38% of the total capsule Ag-110m inventory found on the capsule components [Harp, Demkowicz, and Ploger 2012]) and europium (0.6% of the Compact 6-3-2 inventory found in the DLBL solutions as shown in Table 2). Therefore release from the particles cannot explain the low measured-to-calculated ratios in Table 5. The conclusion is that the discrepancy is because of errors in the calculated fission product inventories for all isotopes except Ag-110m, which was released in large fractions from particles and compacts. This finding is in general agreement with the ratios of calculated versus measured activities determined from gamma scanning of the intact compacts (Harp 2011).

Table 5. Average decay-corrected activities and average ratio of measured to calculated activities. Calculated activities per particle are based on ECAR-958 Rev. 1 and 4,145 particles per compact.

Isotope	Measured activity (Bq)			Measured/Calculated	
	Avg	SD	SD (%)	Avg	SD
Ag-110m	7.45E+3	2.6E+3	35.0%	0.508	0.18
Ce-144	3.74E+7	2.9E+6	7.7%	0.904	0.07
Cs-134	1.58E+6	1.4E+5	9.0%	0.834	0.08
Cs-137	2.53E+6	2.0E+5	7.8%	0.914	0.07
Eu-154	5.28E+4	4.8E+3	9.1%	0.763	0.07
Eu-155	2.63E+4	7.8E+3	29.8%	0.466	0.14
Ru-103	4.13E+7	6.5E+6	15.7%	0.792	0.11
Ru-106	5.72E+6	8.3E+5	14.5%	0.968	0.15
Sb-125	1.26E+5	1.4E+4	11.5%	0.644	0.07
Zr-95	6.17E+7	4.9E+6	8.0%	0.983	0.08

Figures 8 and 9 respectively show the decay-corrected Ce-144 and Cs-137 activity distributions of the 60 gamma counted particles, normalized to the average. The distributions are fairly symmetrical, both with a standard deviation of 8%. The lack of any conspicuous outliers in the Ce-144 distribution indicates that there were no particles with significantly abnormal kernel size, while the lack of conspicuous outliers in the Cs-137 distribution indicates that there were no particles with defective SiC in this small sample of particles, leading to the obvious conclusion that the particle with a defective SiC that was indicated by the DLBL data is not in this sample.

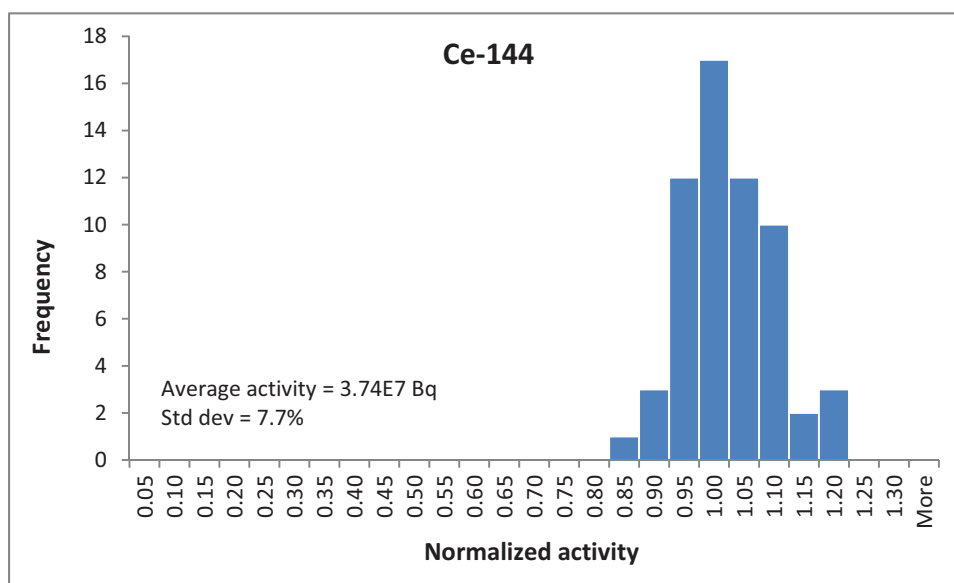


Figure 8. Normalized Ce-144 activity distribution for 60 particles from irradiated Compact 6-3-2.

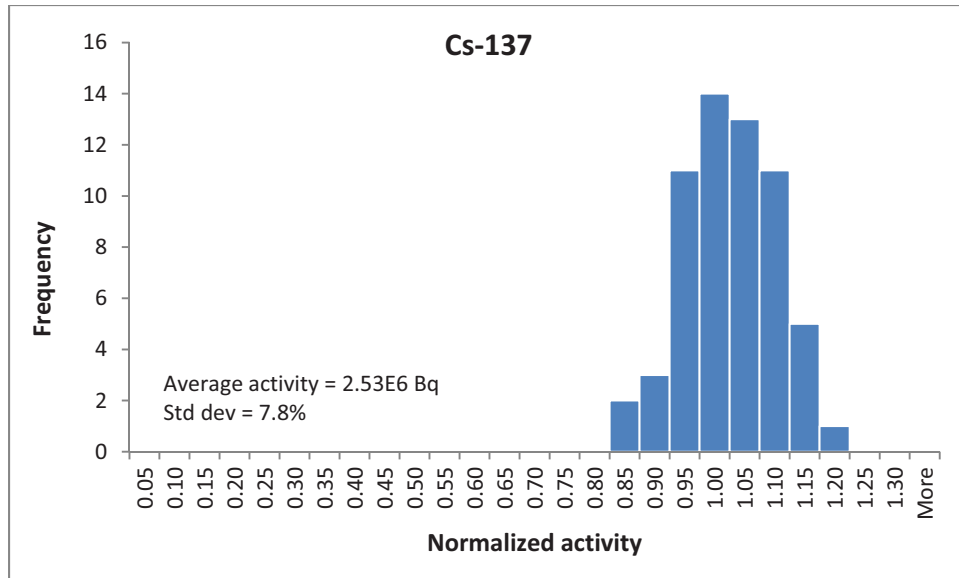


Figure 9. Normalized Cs-137 activity distribution for 60 particles from irradiated Compact 6-3-2.

Release of cerium and cesium from the intact AGR-1 particles has been found to be very low, as indicated by analysis of the AGR-1 capsule components (Harp, Demkowicz, and Ploger 2012) and the DLBL data (Table 2). Thus the distribution of activities in Figures 8 and 9 should be primarily a result of (a) variations in fissile content in the kernel (because of differences in diameter, density, or stoichiometry), (b) variation in Ce-144 or Cs-137 production among particles distributed within the compact volume, and (c) uncertainties in the gamma measurement, but is not expected to be significantly influenced by release from the particles. Dividing the measured activity of an isotope by that of another isotope that is known to be well retained in the particle can minimize the effect of particle-to-particle variation in fissile content and burnup. The distribution of Cs-137/Ce-144 activity ratios, normalized to the mean, is shown in Figure 10. Note that the standard deviation was significantly decreased by taking the ratio of the activities.

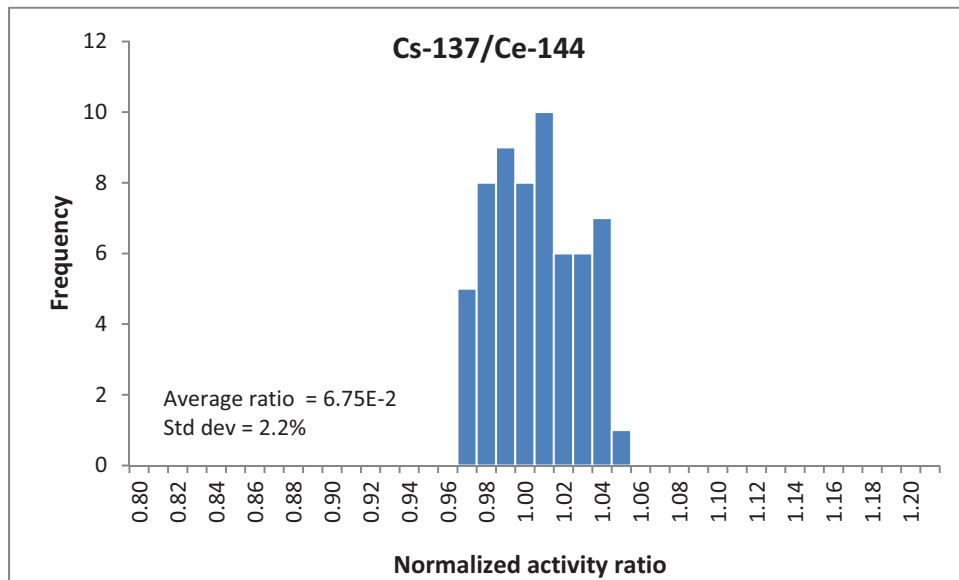


Figure 10. Normalized Cs-137/Ce-144 activity ratio distribution for 60 particles from irradiated Compact 6-3-2.

For the remaining particle gamma counting data presented here, Cs-137 activity was used to minimize the effect of fissile content and burnup variation, instead of Ce-144, which has historically been used for this purpose. The reason for this is that the Cs-137 inventory is a more linear function of burnup and has a long enough half life that it does not significantly begin to reach a saturation concentration during the irradiation, as is the case with Ce-144. Since cesium release from intact particles is very small (much smaller than the uncertainty in the gamma measurement), and no particles with defective coatings are indicated in this sample population, the data should not be influenced by cesium losses from the particles.

The distribution of Ag-110m/Cs-137 decay-corrected activity ratios is given in Figure 11. As indicated in Table 4, no Ag-110m activity was detected for 20 of the 60 particles that were counted. In all cases for which no Ag-110m was detected, the particles had been counted for 2 hours or less. For these particles, the MDA was used as an upper bound estimate of the actual activity in the particles and was used to calculate the Ag-110m/Cs-137 ratio. These particles are plotted separately (shown in red) in Figure 11. It is clear from Figure 11 that the Ag-110m/Cs-137 distributions of the two sets of data cannot be statistically distinguished. Based on this experience, gamma counting of particles from subsequent irradiated compacts will first include exploratory gamma counting to determine counting times required to quantify the Ag-110m activity. (Compact 6-3-2 particles were particularly problematic with regard to measurement of Ag-110m activity, since the combined effect of low burnup compared to other AGR-1 compacts and the relatively high release of silver in many of the particles often resulted in very low Ag-110m activity.)

The Ag-110m/Cs-137 distribution in Figure 11 indicates that silver retention in the particles in Compact 6-3-2 varied over a very wide range. Particles for subsequent microscopic analysis were chosen in part based on their Ag-110m/Cs-137 activity ratios in order to investigate microstructural characteristics related to silver retention. Specific particles selected for microscopic examination are labeled on the distribution of activity ratios in Figure 11, indicating the ratio for each particle.

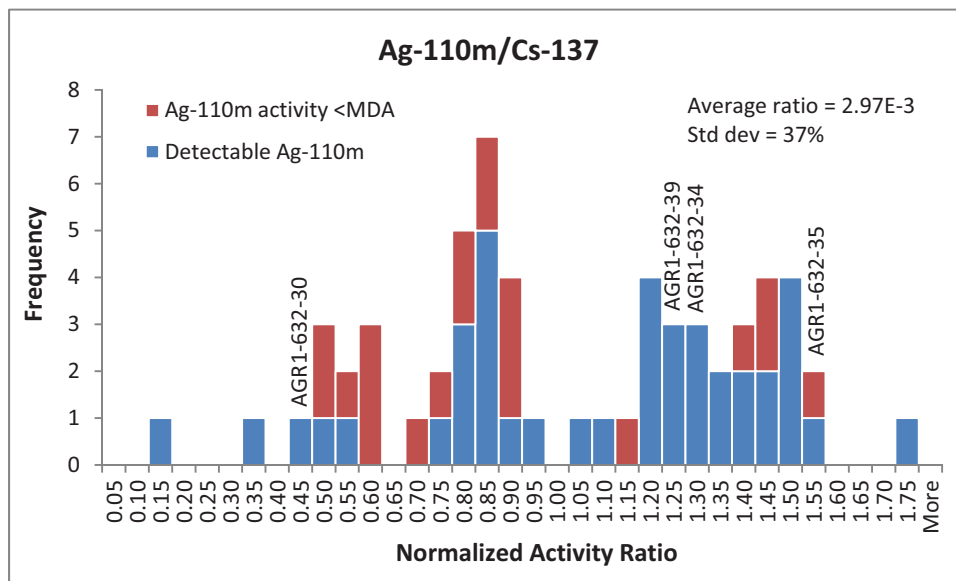


Figure 11. Normalized Ag-110m/Cs-137 activity ratio for Compact 6-3-2. The MDA was used for particles with no measureable Ag-110m activity. These data are plotted separately in red.

A second distribution was prepared to compare the measured Ag-110m activity of each particle (A_i^{Ag110m}) with the predicted activity. The predicted activity for Compact 6-3-2 from Sterbentz 2011 ($A_{632(calc)}^{Ag110m}$) was divided by the average number of particles per AGR-1 baseline compact (4,145) to calculate the predicted activity of Ag-110m per particle ($A_{i(calc)}^{Ag110m}$). A normalization was then applied to this value to minimize the particle-to-particle variation in fissile content (the result of variation in kernel diameter, density, and stoichiometry) and burnup. This was accomplished by dividing by the ratio of measured Cs-137 activity in particle i (A_i^{Cs137}) to average measured Cs-137 activity for all n particles measured ($\sum_{i=1}^n \left(\frac{1}{n}\right) A_i^{Cs137}$). The result is a ratio of measured to predicted Ag-110m activity, normalized for variations in fissile content and burnup. This ratio can be considered as a fraction of the original Ag-110m retained in particle i .

$$\frac{\left[A_i^{Ag110m} / A_{i(calc)}^{Ag110m} \right]}{A_i^{Cs137} / \sum_{i=1}^n \left(\frac{1}{n} \right) A_i^{Cs137}} \quad (3)$$

The resulting distribution of values is presented in Figure 12. The blue and red data sets have the same meaning as in Figure 11. Figure 12 indicates that particles exhibit silver retention ranging from ~10 to 90% of the predicted inventory. This finding is in general agreement with results of extended gamma counting of the intact Capsule 6 compacts for Ag-110m inventory (results not yet published), which indicate that Compact 6-3-2 retained approximately 50% of the predicted Ag-110m inventory.

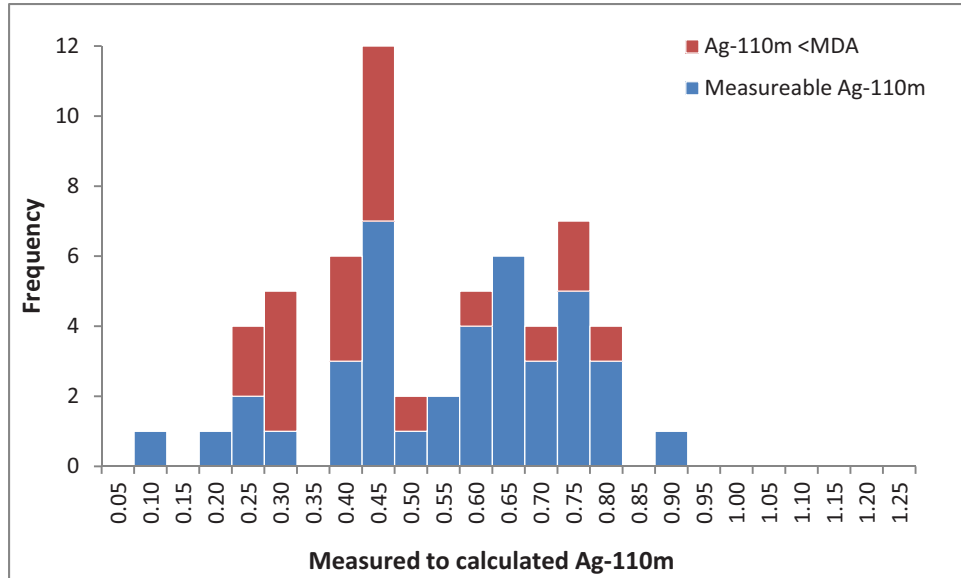


Figure 12. Distribution of the measured-to-calculated Ag-110m activity ratio for irradiated Compact 6-3-2 particles.

The distribution in Figure 12 is particularly instructive, since the large fraction of in-pile Ag-110m release (tens of percent for many of the particles) is significantly higher than the apparent bias in the predicted inventory. For all other fission products, available data (including DLBL data in Section 2, analysis of capsule components discussed in Harp, Demkowicz, and Ploger 2012, and results of gamma scanning intact fuel compacts [Harp 2011]) indicate that total in-pile release from the particles is less than 1%, while the predicted inventory can differ from the actual inventory by tens of percent. As a result, a plot of the adjusted measured-to-calculated activity ratio as shown in Figure 12, would primarily reflect the bias in the calculation and not be indicative of in-pile release. Therefore, the remaining distributions in

this section are presented in terms of simple normalized activity ratios (measured activity of one isotope divided by measured activity of Cs-137, normalized to the mean).

The normalized decay-corrected Eu-154/Cs-137 activity ratio distribution is shown in Figure 13. The distribution is relatively narrow and does not indicate anomalous europium release from any of the particles. One of the particles counted had noteworthy behavior with regard to ruthenium inventory. Figure 14 shows the normalized Ru-106/Cs-137 activity ratio distribution, indicating that one particle (particle AGR1-632-060) had a disproportionately high Ru-106 inventory relative to Cs-137. This particle exhibited similar behavior with regard to Ru-103 as shown in Figure 15 and, to a lesser extent, Sb-125 as shown in Figure 16. No satisfactory explanation for the higher inventory of these isotopes has been developed at this time.

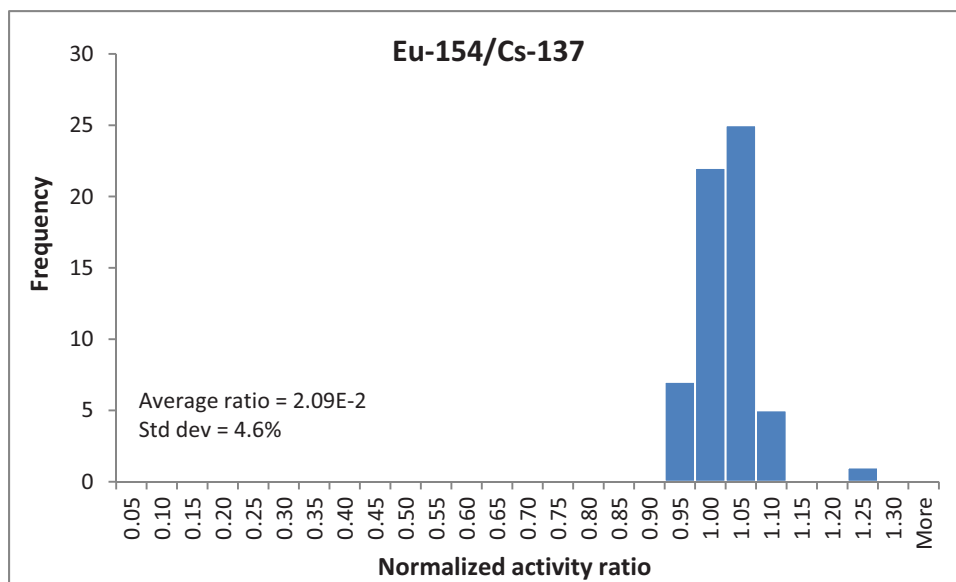


Figure 13. Normalized Eu-154/Cs-137 activity ratio distribution for 60 particles from irradiated Compact 6-3-2.

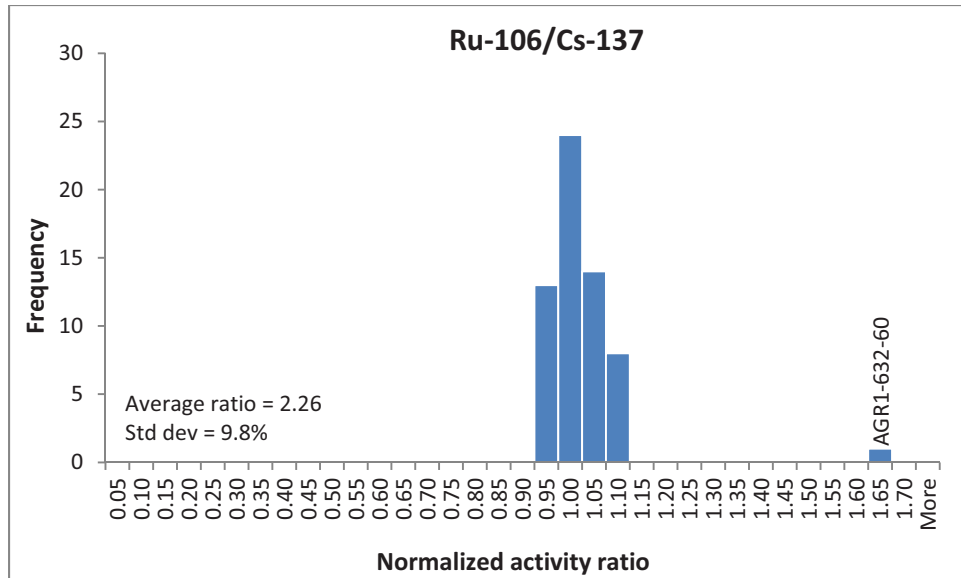


Figure 14. Normalized Ru-106/Cs-137 activity ratio for 60 particles from irradiated Compact 6-3-2. The high outlier is Particle AGR1-632-60.

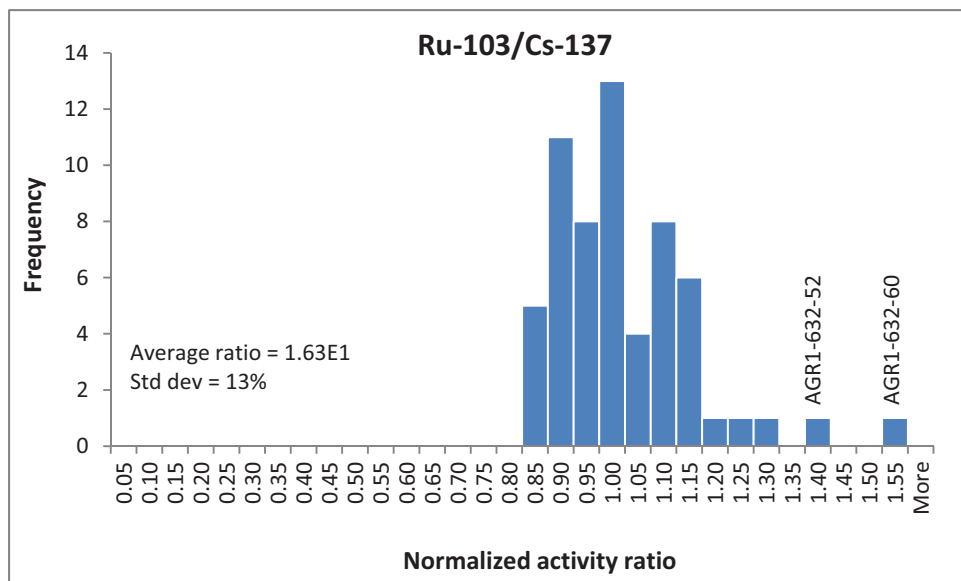


Figure 15. Normalized Ru-103/Cs-137 activity ratio for 60 particles from irradiated Compact 6-3-2. The high outliers are Particle AGR1-632-60 and Particle AGR1-632-52.

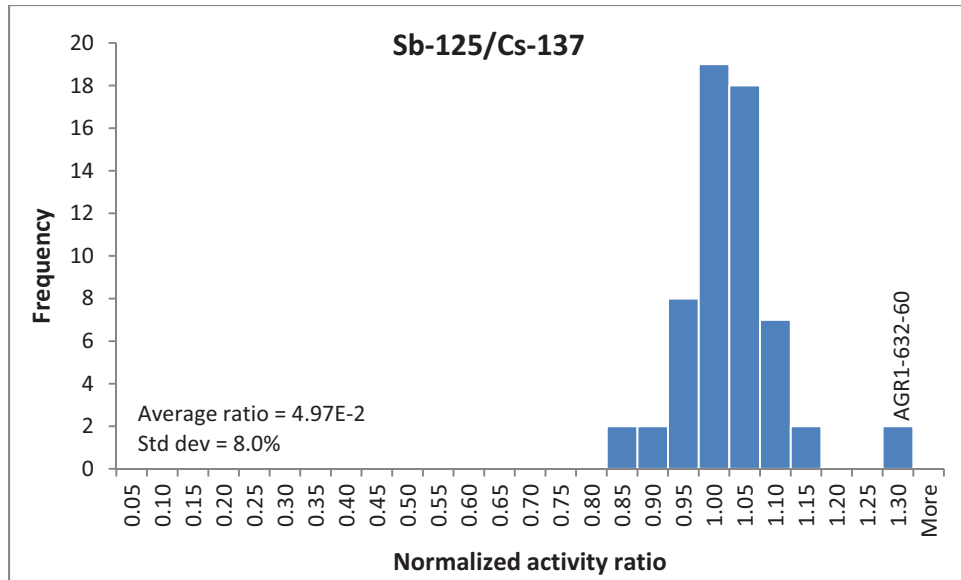


Figure 16. Normalized Sb-125/Cs-137 activity ratio for 60 particles from irradiated Compact 6-3-2.

4. BURNUP ANALYSIS

Burnup measurements on loose particles were performed using two separate methods. The first was a destructive technique based on mass spectrometry data on actinide and fission product inventory in the kernels. Four sets of 20 particles following DLBL analysis were randomly selected using the visual inspection system described in Appendix B. Each set of particles was crushed in a stainless steel mortar and pestle to break the coatings and expose the kernels. Preliminary testing of the first batch of 20 particles indicated that leaching of the crushed particles with hot nitric acid did not result in complete dissolution of the kernels, presumably because of the persistence of less soluble carbide phases. To address this, three sets of the crushed particles were placed in a muffle furnace and heated in air at 400°C for 24 hours to oxidize carbide phases. The crushed and burned particles were then leached in hot 8 M nitric acid for 60 minutes, dissolving the kernels. Preliminary testing of the final three batches of 20 particles indicated that the crush-burn-leach procedure was effective at dissolving all of the kernel material. The solutions generated from dissolving the fuel specimens were analyzed with gamma spectrometry and ICP-MS to measure the concentration of actinides, fission products, and activation products.

The resulting data was transformed into burnup using the “Fission Product Monitor – Residual Heavy Atom” technique. Details of this procedure for determining burnup from ICP-MS measurements are given in Appendix C. Using the ICP-MS results provided in AL Report 93241 (2011), the burnup of three 20-particle batches from Compact 6-3-2 was found to be 11.5, 10.3, and 10.4% FIMA for an average of 10.9% FIMA. The relative error on these values is 5% or about $\pm 0.5\%$ FIMA.

Burnup measurements were also made based on the individual particle gamma counting results presented in Section 3.2. This measurement used the Cs-134/Cs-137 activity ratio and the approach and associated equation described in Harp 2011. The burnup was calculated for each particle using this approach and the average burnup for all 60 particles was calculated to be $11.0 \pm 0.8\%$ FIMA.

These figures agree very well with both the predicted value from Sterbentz 2011 (11.31% FIMA) and the value nondestructively measured with gamma spectrometry of the whole compact and reported in Harp 2011 ($11.0 \pm 0.3\%$ FIMA). The results of burnup values derived from all three experimental methods as well as the calculated value are summarized in Table 6.

Table 6. Measured and calculated burnup values for Compact 6-3-2.

Method	Burnup (% FIMA)	Uncertainty
Prediction ^a	11.31	NA ^b
Gamma spectrometry ^c	11.0	0.3
Irradiated microsphere gamma analysis ^d	11.0	0.8
Mass spectrometry	10.7	0.5

a. Value from ECAR-958 (Sterbentz 2011)

b. No uncertainty value was determined for the calculated burnup.

c. Value determined from whole compact gamma counting data using the Cs-134/Cs-137 ratio method (Harp 2011).

d. Value determined using particle gamma counting data and the Cs-134/Cs-137 ratio method.

5. MICROSCOPY

Microanalysis was performed on individual particles from Compact 6-3-2 to better understand fuel behavior during irradiation. Figure 2 lists the metallurgical sample mounts that were prepared. Several of the mounts involved particles randomly extracted from the population at various stages of the DLBL procedure. In order to investigate potential microstructural characteristics that might be related to fission product releases in-pile, some of the individual Compact 6-3-2 particles selected for detailed microanalysis were chosen based on Ag-110m/Cs-137 activity ratio. Mounts 47T, 48T, and 129T contained particles specifically selected based on IMGA results, including particles from the upper and lower end of the Ag-110m/Cs-137 activity distribution (see Figure 11). Particles AGR1-632-34, -35, and -39 with relatively high Ag-110m/Cs-137 ratios were placed on mount 48T. Particle AGR1-632-30 with a relatively low Ag-110m/Cs-137 ratio was placed on mount 47T. Several particles with Ag-110m/Cs-137 ratios near the middle of the distribution were placed on Mount 129T for potential future analysis. Since Compact 6-3-2 was the first to undergo detailed PIE at INL, much of the met mount preparation described here reveals the developmental nature of the methods used.

Appendix D discusses a classification scheme developed for analyzing internal morphologies of fuel particles exposed in cross-sectioned AGR-1 fuel compacts (Ploger et al. 2012). Type A particles exhibited a continuous gap between the buffer and IPyC layers in the plane of polish, Type B particles showed bonding between the buffer and IPyC layers along the entire interface, and Type AB particles displayed partial debonding between these layers. These three basic types were subdivided according to whether the buffer stayed intact or fractured. Figure D-1 in Appendix D presents representative examples of all six characteristic morphologies.

5.1 Sample Preparation and Ceramography

5.1.1 Mount 21T

Mount 21T was the first irradiated particle mount successfully prepared for ceramography at INL. It contained 19 burned-back AGR-1 fuel particles (outer pyrolytic carbon layer removed) from Compact 6-3-2, randomly selected from available gamma counted particles. Mount 21T consisted of a hollow stainless steel cylinder with narrow, shallow raised steps along the inner and outer diameters. The steel cylinder was placed onto a glass slide to which a thin layer of grease had been applied to hold particles in place while adding epoxy. Particles were poured via a funnel onto the glass slide, followed by Buehler EpoHeat epoxy. Although these particles had been individually identified during the IMGA process, they were mixed during pouring so identification registry was not maintained. After the epoxy was cured at ambient temperature, the glass slide was removed.

Following pneumatic transfer from the Analytical Laboratory to the containment box at the HFEF, the particles were found to have receded slightly into the mount while the epoxy cured. Initial grinding was conducted with Struers MD-Piano 600-grit sandpaper under 40 N of force until the particle exteriors were reached. At this point grinding proceeded more slowly under 20 N of force until frequent periscope examination determined that kernels were just becoming exposed. Exposed kernels meant that radial gaps between buffer and IPyC layers or between kernels and buffers would be open to penetration by back-potted epoxy (also Buehler EpoHeat). Back-potting was conducted by dribbling epoxy onto the mount surface with a manipulator-held eyedropper, followed by placement in a bell jar where vacuum was applied until bubbling could be observed. The bell jar was returned to ambient pressure followed by applying the vacuum two more times, after which the epoxy was cured under hot cell lamps. Figure 17 reveals that the back-potted epoxy wicked into exposed buffer-IPyC gaps quite well, although gas was still occasionally trapped between particles. The back-potting performed as desired since no kernels or buffer-kernel combinations were dislodged from this mount during preparation.

After back-potting, grinding continued with 600-grit sandpaper, first to remove surplus back-potted epoxy and then until periscope examination subjectively suggested that most particles were somewhere near midplane. Final polishing consisted of using Struers MD-1200 sandpaper, 3- μm diamond suspension with a MD-Dac polishing cloth, 1- μm diamond suspension with a MD-Nap cloth, and 0.25- μm diamond suspension with a MD-Chem cloth—all for 6-minute durations under 20 N of force. Fresh sandpaper and polishing cloths were used at each step. After pneumatically transferring the mount to the Leitz metallograph, black and white images were obtained with a 6.6-megapixel Leaf-Volare camera. All particle layers appeared to come into and out of focus at the same time during fine focal adjustments at high magnification, so extra relief of softer layers was minimal. Figure 17 shows only minor residual scratches, plus damage to silicon carbide layers was generally confined to minor indents around particle peripheries.

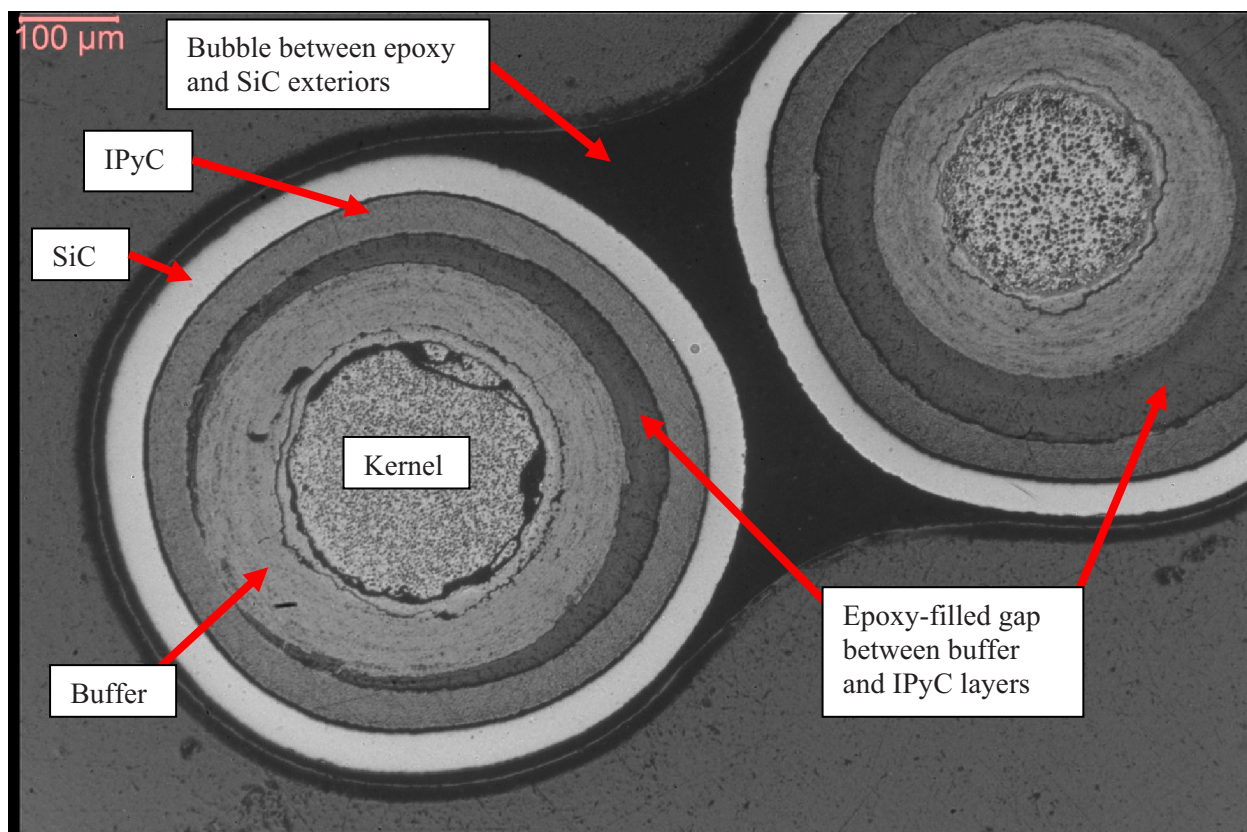


Figure 17. Typical cross sections of burned-back, irradiated fuel particles from Compact 6-3-2 after grinding and polishing Mount 21T.

In Figure 17 the buffer layers densified radially inward to open the gaps filled by back-potted epoxy. The buffer diameter in the left Type ABi particle is noticeably larger than in the right Type Ai particle buffer. This suggests that the kernel/buffer center in the right particle is at a different elevation relative to the SiC and IPyC layers, whereas the small amount of residual buffer-IPyC bonding in the left particle cause the kernel and buffer to be displaced to the left relative to the SiC and IPyC layers. Thus, internal concentricity was lost in both particles after densification of their buffer layers occurred. The off-center kernel/buffer elevation in the right particle exaggerates its apparent buffer-IPyC gap thickness.

Figure 18 provides another example where a small amount of buffer material adhered to the IPyC layer during buffer densification. These stringers of buffer apparently acted as a centering “spider” to keep the kernel and buffer near the same elevation as the IPyC and SiC.

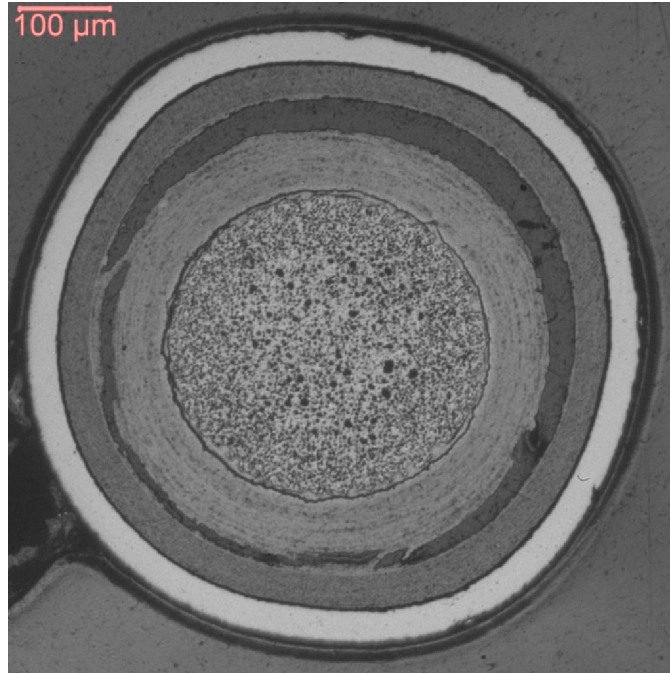


Figure 18. Stringers of buffer material across back-potted epoxy to IPyC layer.

Buffer densification was not always radially inward, as illustrated in Figure 19. The buffer of this Type Bf particle remained attached to the IPyC layer nearly all the way around the circumference. Any radial buffer densification was probably in the outward direction to preserve the buffer-IPyC bonding. Note that one of these buffer cracks propagated into the IPyC layer and extended to the SiC layer. High magnification examination of the SiC at the crack tip revealed no conspicuous damage. This is the only IPyC crack found among irradiated particles from Compact 6-3-2. Substantial pore enlargement occurred inside the kernel.

While little of the kernel entered the buffer cavities in Figure 19, a considerable amount of kernel protruded into one buffer cavity in Figure 20. More kernel protrusion at the lower left suggests that this buffer fracture occurred earlier than the fracture at the upper right, allowing more time for the kernel to protrude into the opening. Buffer-IPyC debonding appears complete in this Type Af particle (at least in the plane of polish), so kernel swelling may have pushed the buffer fragments apart, perhaps partially closing a buffer-IPyC gap that existed before kernel swelling.

As in Figure 19, kernel pores in Figure 20 are much larger than in Figure 17 and Figure 18. Larger pores may indicate more coalescence, but larger pores may also be related to less constraint on kernel swelling after buffer fracture. However, Figure 21 presents one example to the contrary, where radial buffer fractures occurred without appreciable pore enlargement. In the case of Figure 21, kernel swelling may still have been constrained by a residual buffer material blocking kernel protrusion into cavities. Another interpretation of Figure 21 is that buffer fracturing in this particle may have occurred late during irradiation, allowing little time for pore enlargement and kernel protrusions into buffer cavities.

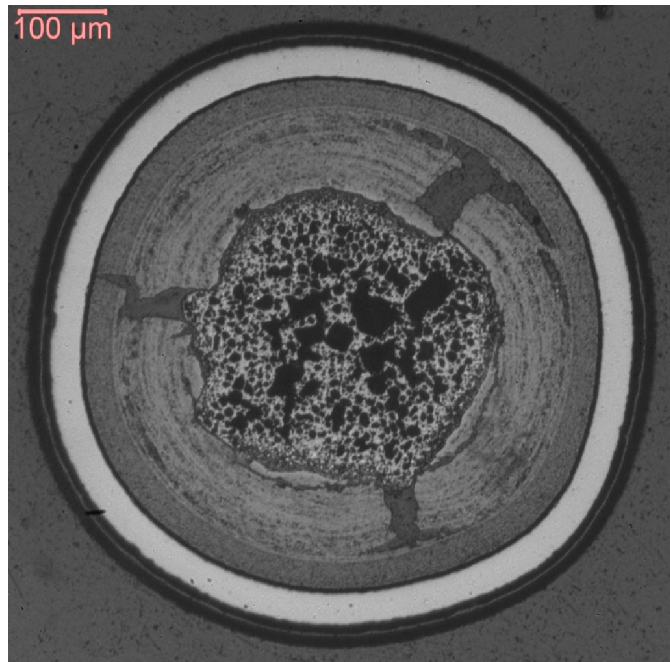


Figure 19. Radial buffer cracks, one of which evidently induced an IPyC fracture on left side.

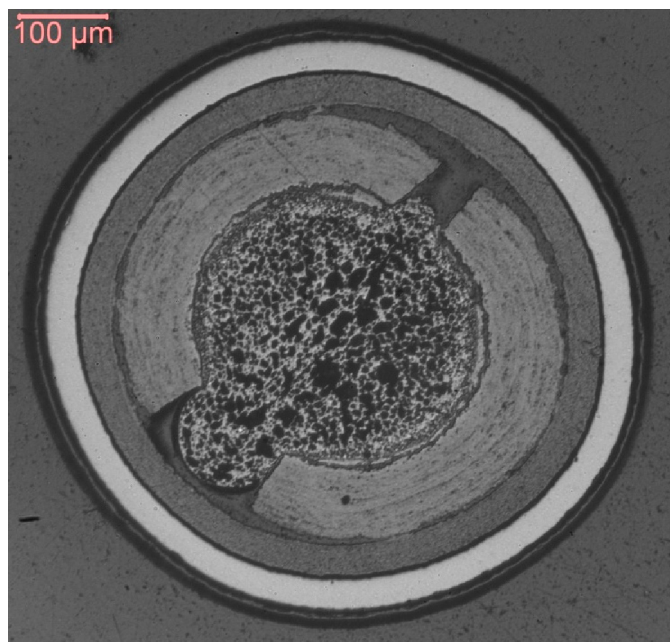


Figure 20. Kernel protrusion into buffer fractures.

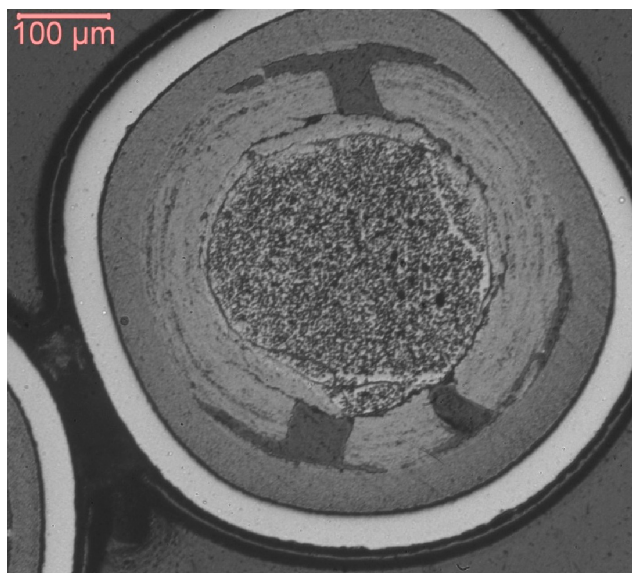


Figure 21. Wide buffer fractures without large kernel pores.

5.1.2 Mount 22T

More difficulty was encountered subsequently when preparing Mount 22T, which was loaded with 47 randomly selected burned-back particles from Compact 6-3-2. An attempt was made to follow the same sequence used for Mount 21T, but the epoxy portion of this mount slid out slightly from the stainless steel cylinder during pneumatic transfer and the slippage was not detected until after the first grinding step. Because the particle-containing epoxy protruded, none of the grinding force was applied to the stainless steel and grinding proceeded much faster into the Mount 22T particles during the first grinding step than expected. Two particles were entirely dislodged, eight of the remaining 45 particles lost their kernels and buffers, and extensive fracturing occurred in the silicon carbide layers before back-potting could be conducted. (The possibility of epoxy slippage was later precluded on particle mounts by machining a deep groove into the interior of the mount cylinders to lock the epoxy into place.) The Mount 21T grinding and polishing sequence was resumed after back-potting Mount 22T, but new scratches emerged during each step as SiC fragments broke free. A second back-pot was done, followed by more grinding with 600-grit sandpaper in an attempt to go beyond the damaged SiC. However, more SiC scratches emerged during the subsequent grinding/polishing operations, which left a final surface of unsatisfactory quality. Figure 22 illustrates extensive SiC fracturing and scratches in interior layers, along with a missing kernel/buffer in the left particle. The appearance of the right particle in Figure 22 is typical of the 37 particles in Mount 22T that retained their kernels and buffers. Scratches occasionally compromised exam objectives, such as searching for IPyC cracks, but no obvious IPyC cracks were found in Mount 22T particles.

Despite the extensive preparation damage, internal morphologies could still be studied in the vast majority of Mount 22T particles that retained their kernels and buffers. Particles generally resembled those already described from Mount 21T, but four particles from Mount 22T revealed no epoxy-filled gap between buffer and IPyC or between kernel and buffer, as well as no cracks across buffer layers. A Type Bi example is presented in Figure 23, where concentricity of the kernel and all coating layers was maintained in the absence of radial gap formation. Because the buffer remained bonded to the IPyC around the entire circumference, any buffer densification occurred radially outward. Meanwhile, the kernel diameter evidently expanded to fill the area created by the outward buffer densification. Kernel pores are relatively large in Figure 23 and in the other three similar particles from Mount 22T, which may be associated with less constraint on kernel swelling. Figure 23 resembles Figure 19 in most regards, excepting the radially oriented buffer cracks in Figure 19.

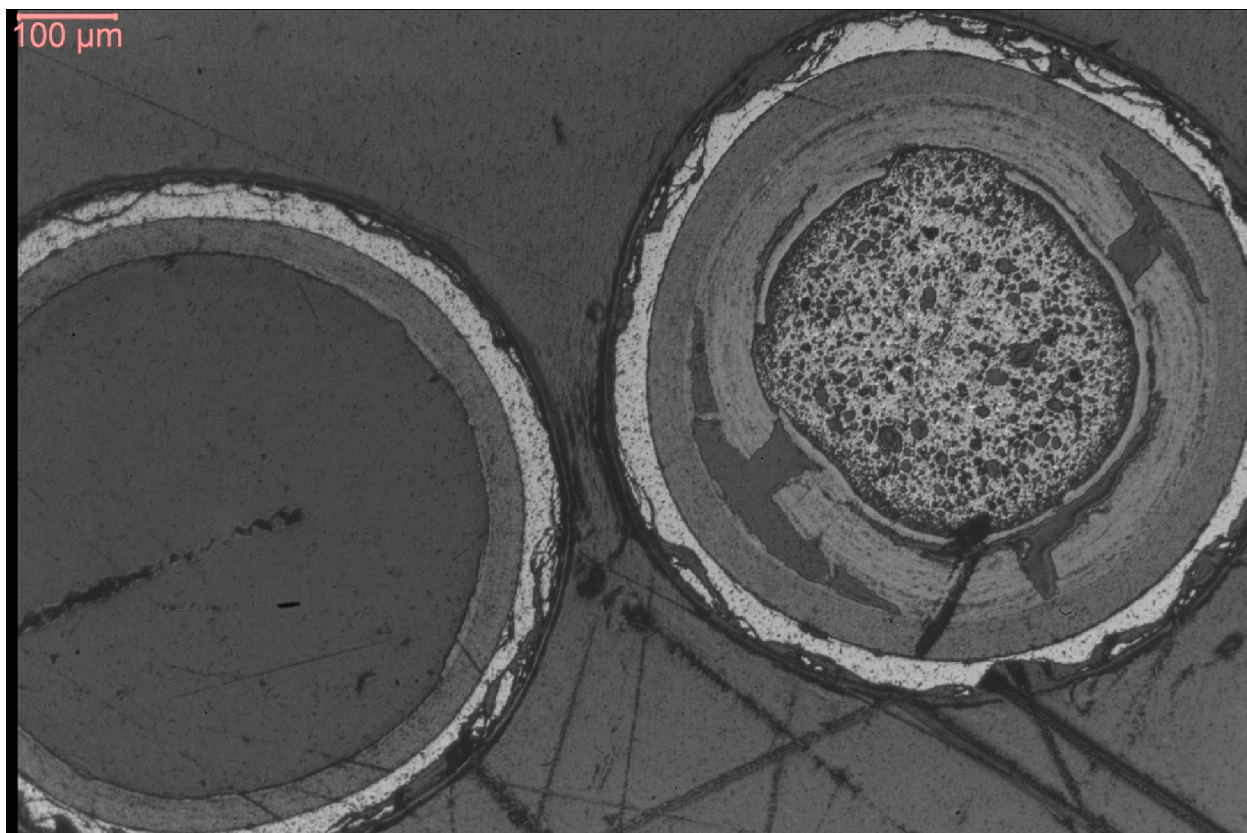


Figure 22. Preparation damage in Mount 22T, with kernel and buffer dislodged from left particle.

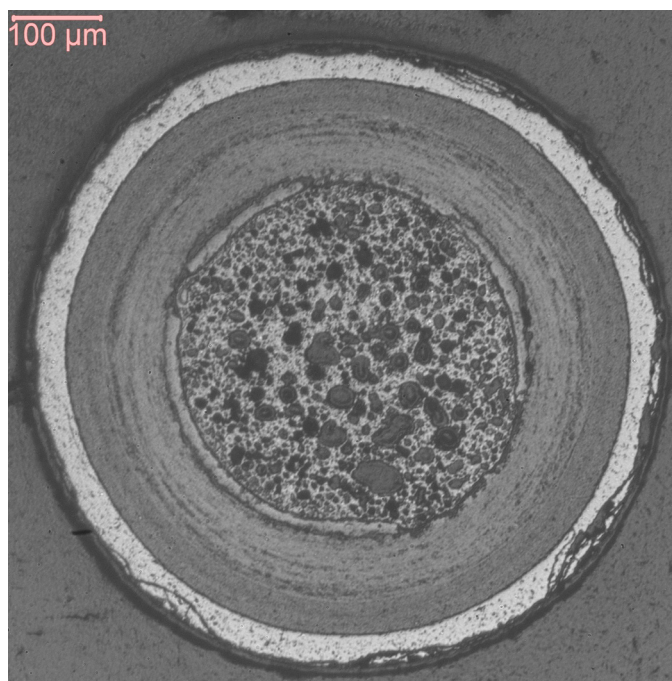


Figure 23. Type Bi morphology found in four Mount 22T particles.

Mount 22T had 18 particles with fractured buffers. A Type ABf example is presented in Figure 24. Kernel pores typically enlarged in these cracked buffer particles, perhaps reflecting less constraint on kernel swelling.

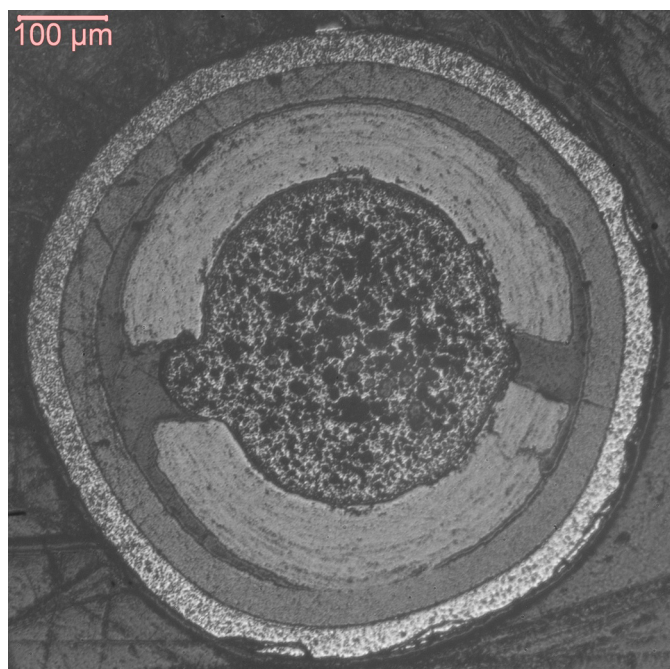


Figure 24. Typical fractured buffer particle in Mount 22T.

5.1.3 Mounts 47T and 48T

Mount 47T was loaded with Particle AGR1-632-30, which had a low Ag-110m/Cs-137 gamma count ratio. Particles AGR1-632-34, -35, and -39 with relatively high Ag-110m/Cs-137 ratios were placed in Mount 48T. Fewer particles were loaded than in Mounts 21T and 22T to diminish radiation dose during handling to enable eventual examination at the MFC Electron Microscopy Laboratory. Both mounts included stainless steel cylinders of identical design to those used in Mounts 21T and 22T. However, thin double-sided tape was stretched across the mount bottoms and backed with a glass slide to hold particles in place, rather than using a thin layer of grease on the slide. In addition, the three particles were loaded one at a time into Mount 48T and their individual positions were recorded photographically so that their identities were maintained. The thin tape could pull inward as the epoxy cured and shrank, so Mount 48T particles were not perfectly aligned with the mount base as intended and they were not exactly at the same elevation along the curved epoxy surface. Consequently, despite the tape, it was still necessary to grind beyond the stainless steel steps to approach particle midplanes, which required slow removal of the full 0.25-inch stainless steel wall thickness.

Mount 48T was ground with a Struers MD-Piano 600-grit disk using 10-20 N of force until kernels were just exposed in two of three particles (not possible in all three because of staggered elevations). At this depth, the buffer-to-IPyC gap from buffer densification was opened in all three particles for back-potting to stabilize the kernels and buffer layers. Coarse grinding then continued with a 600-grit disk until two of three particles were approximately at midplane. Fine grinding was then conducted with an MD-Piano 1200-grit disk for 2 minutes using 20 N of force. Polishing began with a 3-μm diamond suspension on a Struers MD-Dac cloth using 20 N of force, which continued for a total of 6 minutes until periscope viewing indicated that grinding scratches were no longer conspicuous in the epoxy. Silicon carbide layers also became noticeably reflective. Polishing continued with a 1-μm diamond suspension on

an MD-Nap cloth for 6 minutes at 20 N of force, whereupon the epoxy also became shiny. Polishing was completed with a 0.25- μm diamond suspension on an MD-Chem cloth, again for 6 minutes at 20 N.

The same approach was attempted on Mount 47T. The single particle was initially located deep inside the epoxy, so a substantial amount of stainless steel had to be ground away to expose the particle. Nevertheless, the particle was finally exposed and ground until the kernel was visible for back-potting of the buffer-to-IPyC gap. After removal of surplus back-potted epoxy, coarse grinding continued until Mount 47T appeared ready for fine grinding and polishing. Several weeks passed before preparation could resume. Fine grinding with a 1200-grit disk failed to remove scratches. Careful observation established that the epoxy had gradually retreated into the mount, at which time it was learned that heat-curing had not been performed at the Analytical Laboratory on any of the Compact 6-3-2 mounts. Coarse grinding had to be conducted again with a 600-grit disk until sufficient stainless steel was removed to reach the particle. Force was increased to 30 N to expedite the lengthy process. Unfortunately, the last coarse grind went far deeper into the particle than desired (beyond midplane), the kernel was lost, and breakup of the hard kernel resulted in deep scratches in remaining layers and some fractures in the silicon carbide. Another back-pot was performed in an attempt to salvage the remaining layers, especially the silicon carbide. Poor control over grinding depth during removal of surplus epoxy again resulted in removal of far more particle than desired. All that remained was the crown of the silicon carbide. Nevertheless, the remnant was fine ground and polished as described above for Mount 48T to investigate the microstructure of the SiC and fission product distribution within the layer at the Electron Microscopy Laboratory. The final configuration is displayed in Figure 25, where the darker area in the middle of the SiC is a shallow depression where the original IPyC-SiC interface existed. (Difficulties with Mount 47T resulted in adding a furnace cure for the epoxy at the Analytical Laboratory. In addition, the thin tape was replaced with a thick, stiff double-sided tape that adhered much better to the glass slide and resisted being pulled into the mount as the epoxy was cured.)

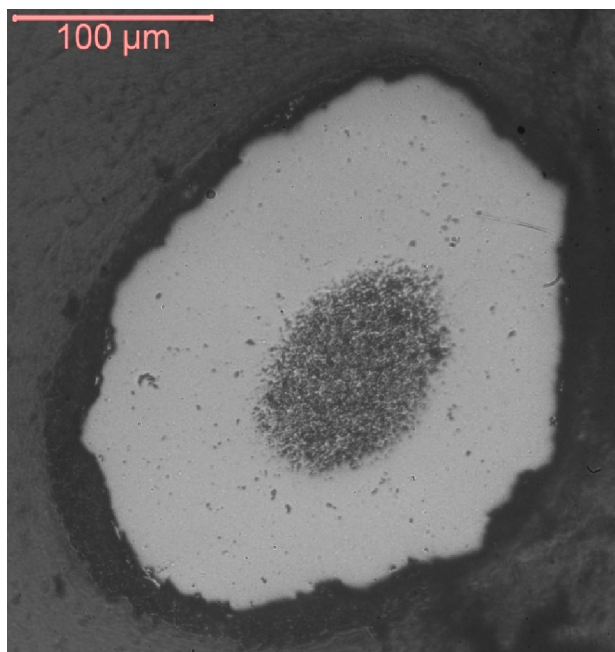


Figure 25. Silicon carbide remnant from Particle AGR1-632-30 in Mount 47T.

Two of the three Mount 48T particles are shown in Figure 26. Buffer and IPyC layers separated in both Type Ai particles. However, some small buffer fragments remained attached to the IPyC interior in Particle AGR1-632-39, peeling away from the remainder of the buffer as it densified inward.

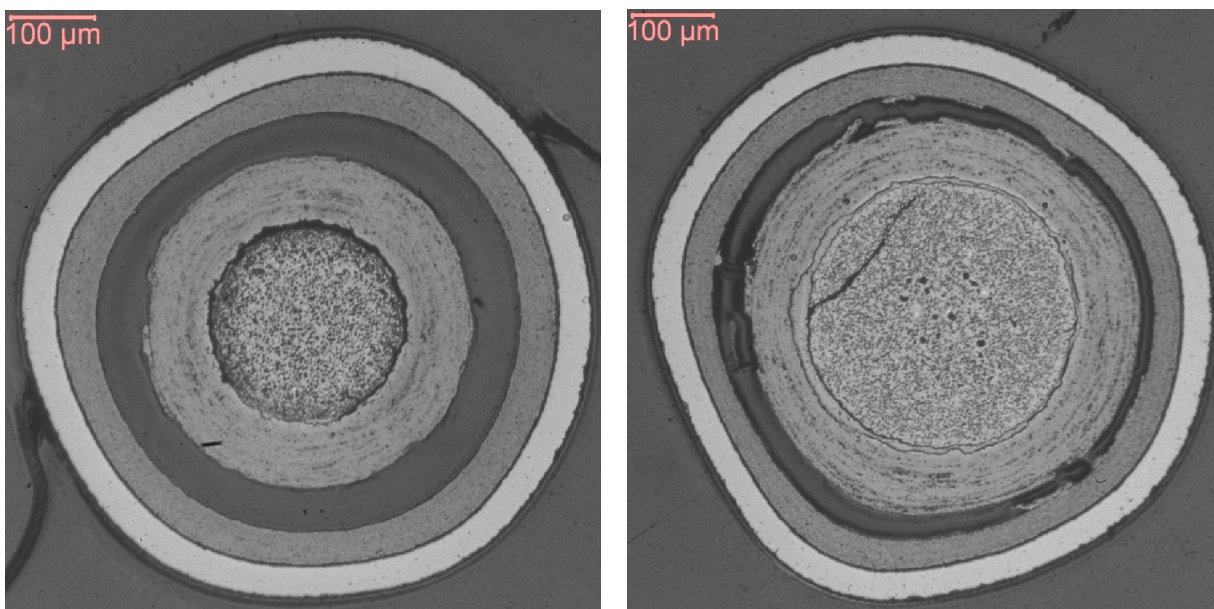


Figure 26. Particles AGR1-632-34 (left) and AGR1-632-39 (right) within Mount 48T.

Remaining Mount 48T Particle AGR1-632-35 is displayed in Figure 27. Buffer and IPyC remained bonded around their entire interface of this Type Bi particle, as in Figure 23. Fission gas pores are larger than the particles in Figure 26, which perhaps is associated with less imposed constraint on kernel swelling as a consequence of radially outward buffer densification.

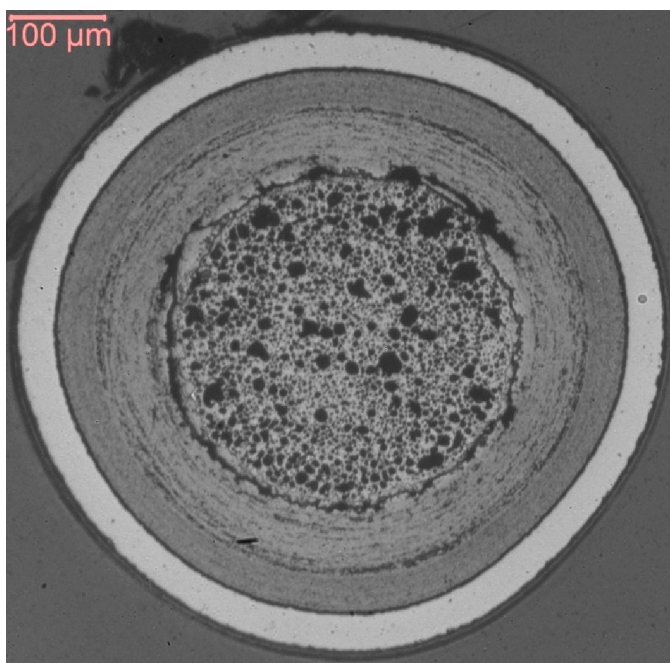


Figure 27. Mount 48T Particle AGR1-632-35, where the buffer remained bonded to the IPyC layer.

5.1.4 Summary Observations on Compact 6-3-2 Particles

All Compact 6-3-2 particles were classified excepting Particle AGR1-632-30 in Mount 47T and the ten severely damaged particles in Mount 22T. Results are displayed in Figure 28. Figure 29 indicates that the classification results are reasonably consistent with those from cross-sectioned Capsule 6 compacts (Ploger et al. 2012). Minor differences among the three Capsule 6 compacts in as indicated in Figure 29 probably are not the results of slight differences in neutron exposure or irradiation temperature, because no obvious relationships between particle types and irradiation conditions were uncovered among the six cross-sectioned AGR-1 compacts that had much larger differences in irradiation conditions (Ploger et al. 2012).

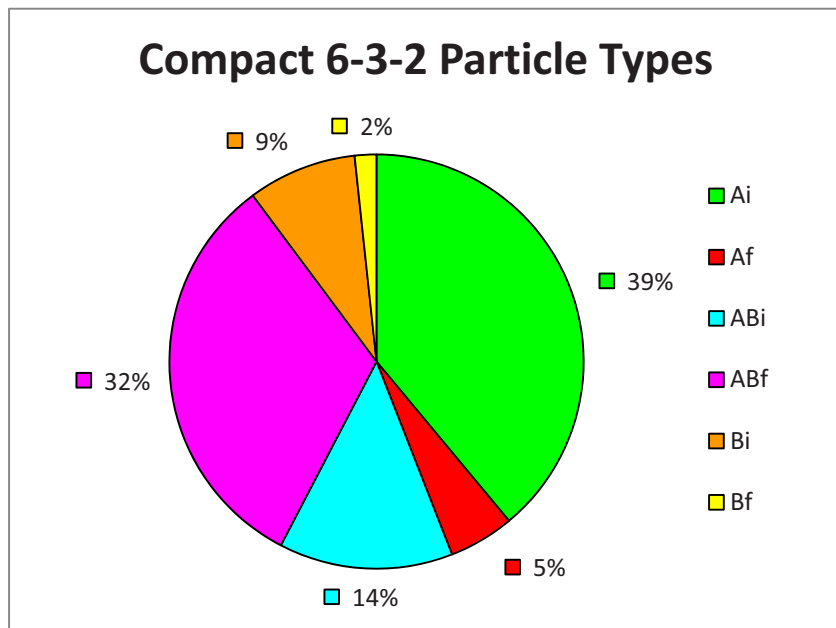


Figure 28. Distribution of particle types found in Compact 6-3-2 Mounts 21T, 22T, and 48T.

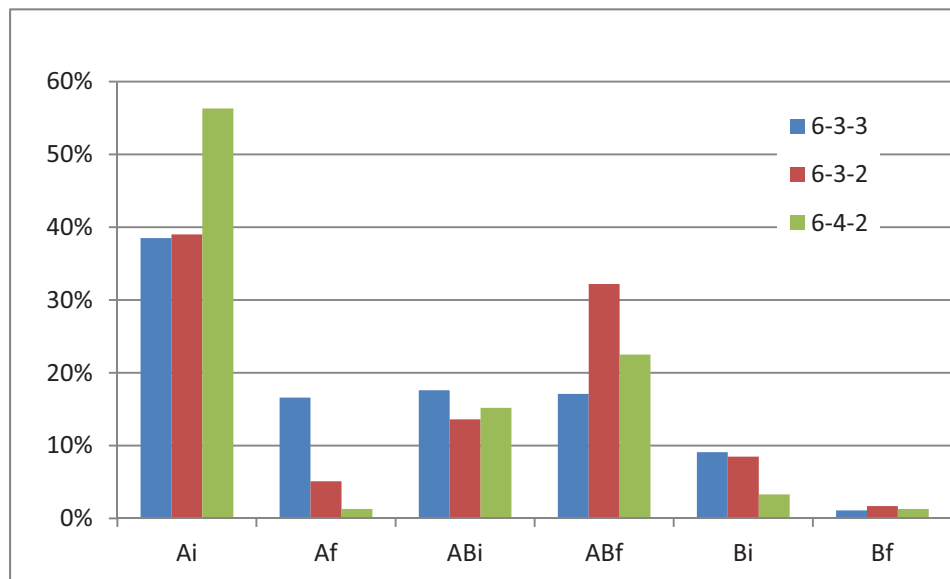


Figure 29. Distribution of particle types among compacts from AGR-1 Capsule 6.

A general tendency was observed for pore enlargement in kernels within Type B particles from Compact 6-3-2, where buffers evidently densified radially outward, and in kernels surrounded by fractured buffers. Meanwhile, kernel pores typically appeared smaller within intact, inwardly densified buffers (Type Ai and Type ABi particles). This observation agrees with tendencies found in particles from cross-sectioned AGR-1 compacts (Ploger et al. 2012), where pore enlargement was clearly tied to less buffer-imposed constraint on kernel swelling.

Diameter measurements were attempted on several Compact 6-3-2 particles by fitting circles to manually selected points after calibrating the camera pixel size to a stage micrometer (glass reticle) on the metallograph. Although some kernel swelling and buffer densification were indicated by these efforts, measurement accuracy was compromised by the combination of staggered particle elevations within individual amounts, uncertain proximity to midplane, nonconcentric kernels and buffers in particles with a buffer-IPyC gap, and variability in as-fabricated particle sizes. Consequently, none of these diameter values are reported here.

5.2 Electron microscopy

Mounts 47T and 48T were transferred to the MFC Electron Microscopy Laboratory for detailed microscopic and elemental characterization, including scanning electron microscopy, focused ion beam sample preparation, transmission electron microscopy, energy dispersive x-ray spectroscopy, and wavelength dispersive spectroscopy. This analysis focused on a broad range of particle characteristics, including kernel microstructure and composition, basic coating and coating interface microstructures, and fission product locations and elemental composition and crystallographic properties of fission product precipitates. A detailed report has been prepared that discusses aspects of coating characterization and identification of fission product precipitates in the IPyC and SiC layers (van Rooyen et al. 2012).

6. RESULTS SUMMARY

The key findings from destructive PIE of Compact 6-3-2 are as follows:

- A single particle with a defective SiC layer was found during DLBL analysis, primarily evidenced by the uranium equivalent of roughly one kernel in the first post-burn leach solution. This finding is in general agreement with data on cesium inventory in the Capsule 6 graphite holder (Harp and Ploger 2011), which indicated a cesium hot spot in the graphite holder at the original location of Compact 6-3-2. The net result suggests that gamma scanning of the AGR-1 graphite holders using the HFEF Precision Gamma Scanner was capable of detecting the released Cs-134 and Cs-137 inventory from a single particle.
- A relatively large amount of europium was released from the particles and retained in the compact matrix during the irradiation, equivalent to the inventory of 20 to 25 particles (~0.6% of the total compact inventory).
- While it is clear from the IMGA results that a significant fraction of silver was released from certain particles in Compact 6-3-2 during the irradiation, it appears that this was not well retained in the compact matrix, as the inventory of Ag-110m in the DLBL solutions was approximately equivalent to the inventory of a single particle (compact fraction of 2.2×10^{-4}), with a large fraction of this appearing the first post-burn leach solution where a single kernel was dissolved.
- The release of Ag-110m from individual particles appears to have varied over a wide range, with selected particles retaining as much as 80-90% of the original predicted inventory, while other particles retained <25% of the original inventory. The average measured-to-calculated ratio of Ag-110m for the 60 particles gamma counted was 0.51, indicating that, on average, the particles lost ~50% of the original Ag-110m inventory. The high release of silver from the particles is in general agreement with the results of gamma scanning the other compacts from Capsule 6, which suggest that the total release from Compact 6-3-2 should be ~50% or higher.
- There was no evidence from the particle gamma counting data to suggest that any particles exhibited a release significantly in excess of ~1% of any fission product other than Ag-110m. The distributions of measured activities of other fission products were symmetrical and had relatively low standard deviations.
- The agreement between burnup measurements from three different methods—gamma spectrometry of whole compacts, gamma spectrometry of individual particles, and mass spectrometric measurements of dissolved kernels—was very good, with the average values from each method ranging from 10.7-11.0 % FIMA. The maximum relative deviation of the measured values from the predicted value based on physics calculations was 5%.
- Optical microscopy of particle cross-sections showed that the particles exhibited a range of behaviors based on buffer-IPyC interface behavior, with the interface ranging from fully intact to fully debonded. The buffer layers have visible fractures in ~40% of the particles examined.
- Fuel kernels often protruded into the gaps caused by buffer fractures. Kernels also often exhibited enlarged pores, possibly the result of kernel swelling and pore coalescence during irradiation.

7. LESSONS LEARNED AND RECOMMENDATIONS

Because Compact 6-3-2 was the first coated particle fuel to undergo PIE at INL in several decades, this represented a general shakedown of methods and approaches. In general, the PIE equipment and techniques developed for the NGNP program and discussed in this report worked extremely well. Some of the key lessons learned as a result of the experience gained with Compact 6-3-2 and recommendations for future TRISO fuel compact PIE are provided in this section.

It was discovered during gamma counting of individual particles that the Ag-110m inventory of certain particles was often difficult to quantify, in particular if total count times ≤ 2 hours per particle were used. Based on analysis of the data from all 60 particles, it was concluded that this was primarily a consequence of (a) the low burnup of Compact 6-3-2 relative to other AGR-1 compacts, which significantly lowered predicted Ag-110m activity per particle (predicted Ag-110m activity in Compact 6-3-2 was the second lowest of all 72 AGR-1 compacts, and $\sim 31\%$ of the average compact activity), and (b) relatively high silver release from selected particles, which further significantly reduced the Ag-110m activity per particle. The detection threshold of any isotopic activity in a particle will necessarily be determined by the specific experimental variables (including counting geometry, detector efficiency, total gamma counts from other isotopes in the particles, and gamma counts from background contamination). So, while longer counting times typically can reduce the MDA, there will always be a practical minimum that can be achieved with reasonable counting times (for the INL approach to gamma counting, it has been determined that counting times of approximately 6 hours or less will be required in order to process 60 particles in an acceptable timeframe). It was determined based on Compact 6-3-2 results that a counting time between 2 and 12 hours may have been capable of quantifying the Ag-110m activity in all of the particles analyzed. For analysis of future compacts, it is recommended that a screening analysis be performed on a subset of particles to determine the approximate counting duration sufficient to quantify Ag-110m activity.

Considerable difficulty was encountered during preparation of ceramographic mounts. Much of this difficulty was associated with the inability to keep particles evenly located at the bottom of the mounts after applying epoxy. A thin layer of grease proved ineffective at holding all particles onto the glass slide when epoxy was poured. Somewhat better control was achieved when the grease was replaced with thin double-sided adhesive tape, but the tape would still deform inward as the epoxy cured, resulting in uneven particle elevations. Ultimately, a thick, stiff double-sided tape was used to keep particles at the same elevation. Furthermore, the epoxy did not adhere to the stainless steel mount sides and occasionally relocated within the mount, which required additional grinding and time-consuming, problematic removal of stainless steel mount walls. Incorporation of an internal groove locked the epoxy at the groove elevation, but the epoxy surface still retreated inside the mount as the epoxy gradually cured under heat from hot cell lamps. Consequently, a furnace cure also had to be implemented where mounts were loaded to stabilize the epoxy before any grinding commenced. Another improvement that has been adopted subsequent to preparation of the Compact 6-3-2 particle mounts was to diminish the amount of stainless steel that must be removed to reach particle midplanes during grinding, which lowered the grinding force and provided more control over grinding depth. Two approaches are being used in this regard: (1) adding a deep recess to the bases of stainless steel mounts, leaving only a narrow step around the mount exterior for grinding (conductive mounts with a small number of particles destined for electron microscopy) and (2) using mounts made from relatively soft Micarta (larger ensembles of particles intended only for optical microscopy).

Attempted diameter measurements on particle images were hampered by large uncertainties from several sources. Improvements on taping and epoxy curing will help to keep particles at a consistent elevation within mounts. Moreover, a dial indicator-based mount thickness gauge has been developed to reduce the subjectivity in determining proximity to midplane of SiC layers.

Lastly, at least two back-pots are being performed as particles are ground toward midplane, the first as gaps are opened between buffers and IPyC layers and the second as kernels are initially exposed. The second back-pot was added to provide more assurance of kernel stabilization in Type B particles and in particles with fractured buffers.

8. REFERENCES

- Barnes, C.M., W.C. Richardson, D. Husser, M. Ebner, 2008, "Fabrication processes and product quality improvements in Advanced Gas Reactor UCO kernels," HTR2008-58039, *Proceedings of the 4th International Topical Meeting on High Temperature Reactor Technology, HTR2008, Washington, DC, USA, September 28–October 2, 2008*.
- Chadwick, M.B., et al., 2011, "ENDF/B-VII.1 Nuclear Data for Science and Technology: Cross-Sections, Covariances, Fission Product Yields and Decay Data," *Nuclear Data Sheets*, Vol. 112, pp. 2887–2996. Specific decay data accessed at: <http://www.nndc.bnl.gov/exfor/endl00.jsp>.
- Demkowicz, P.A., 2010, "AGR-1 Post-Irradiation Examination Plan," PLN-2828, Rev 1, March 2010.
- Demkowicz, P.A., L. Cole, S. Ploger, P. Winston, 2011, *AGR-1 Irradiated Test Train Preliminary Inspection and Disassembly First Look*, INL/EXT-10-20722, January 2011.
- Grover, S.B., D.A. Petti, J.T. Maki, 2010, "Mission and status of the first two next generation nuclear plant fuel irradiation experiments in the Advanced Test Reactor," ICONE18-30139, *Proceedings of the 18th International Conference on Nuclear Engineering, Xi'an China, May 17–21, 2010*.
- Grover, S.B., 2010, "Completion of the First NGNP Advanced Gas Reactor Fuel Irradiation Experiment, AGR-1, in the Advanced Test Reactor," Paper 104, *Proceedings HTR-2010, Prague, Czech Republic, October 18–20, 2010*.
- Harp, J.M., 2011, "Analysis of Individual Compact Fission Product Inventory and Burnup for the AGR-1 TRISO Experiment Using Gamma Spectrometry," ECAR-1682, September 2011.
- Harp, J.M., and S.A. Ploger, 2011, "Examination of Graphite Fuel Compact Holders for the AGR-1 TRISO Experiment Using Gamma Spectrometry," ECAR-1709, November 2011.
- Harp, J.M., P.A. Demkowicz, S.A. Ploger, 2012, "Post-irradiation Examination and Fission Product Inventory Analysis of AGR-1 Irradiation Capsules," HTR2012-3-006, *Proceedings of the 6th International Topical Meeting on High Temperature Reactor Technology HTR2012, October 28–November 1, 2012, Tokyo, Japan*.
- Hawkes, G.L., 2012, "AGR-1 Daily As-Run Thermal Analyses," ECAR-968 Rev. 3, May 2012.
- Hunn, J.D., and R.A. Lowden, 2006, *Data Compilation for AGR-1 Baseline Coated Particle Composite LEU01-46T*, ORNL/TM-2006/019, August 2006.
- Hunn, J.D., F.C. Montgomery, and P.J. Pappano, 2006, *Data Compilation for AGR-1 Baseline Compact Lot LEU01-46T-Z*, ORNL/TM-2006/507 Rev 0, August 2006.
- Maki, J.T., 2009, *AGR-1 Irradiation Experiment Test Plan*, INL/EXT-05-00593, Rev. 3, October 2009.
- Ploger, S.A. P.A. Demkowicz, J.D. Hunn, 2012, *Ceramographic Examinations of Irradiated AGR-1 Fuel Compacts*, INL/EXT-12-25301, Rev. 1, September 2012.
- Simonds, J., 2010, "Technical Program Plan for the Next Generation Nuclear Plant/Advanced Gas Reactor Fuel Development and Qualificaion Program," PLN-3636, September 2010.

- Sterbentz, J. W., 2011, "JMOCUP As-Run Daily Depletion Calculation for the AGR-1 Experiment in the ATR B-10 Position," ECAR-958, Rev. 1, August 2011.
- van Rooyen, I.J., B. Miller, D. Janney, J. Riesterer, P. Demkowicz, J. Harp, S.A. Ploger, 2012, *Electron Microscopic Examination of Irradiated TRISO Coated Particles of Compact 6-3-2 of AGR-1 Experiment*, INL/EXT-11-23911, December 2012

Appendix A

Deconsolidation-Leach-Burn-Leach Procedure

Appendix A

Deconsolidation-Leach-Burn-Leach Procedure

The majority of the functions performed by the MFC Analytical Laboratory in support of the Advanced Gas Reactor (AGR) post-irradiation examination (PIE) occur in the MFC-752 Hot Cells. Each of the six cells, also known as the Junior Caves, has a nominal 6 × 5-ft floor area, 2-ft-thick concrete walls, a shielding window, and two Central Research Laboratory manual manipulators. They are supplied with compressed air, vacuum, and miscellaneous electrical and electronic connections integral to the cell. Tubing is available to provide liquid chemicals if direct flow is required. The cells have an air atmosphere and are maintained at a negative pressure to provide contamination control. Materials from the Hot Fuels Examination Facility or the Fuel Conditioning Facility may be received via pneumatic rabbit in Analytical Hot Cell 1 and transferred to other hot cells by a chain-driven cart that connects Hot Cells 1 through 6.

The Analytical Laboratory performs the deconsolidation and leach-burn-leach cycles according to Laboratory Instruction AL-5000-LI-018, “Electrolytic Deconsolidation and Leach-Burn-Leach Method.” The task is to deconsolidate the compact, electrochemically breaking down the compact carbonaceous matrix and releasing the TRISO particles. The particles are then subjected to two 24 hour cycles submerged in hot concentrated nitric acid in a Soxhlet extractor. The particles are transferred to a muffle furnace, where the OPyC layer is oxidized at 750°C in air for 72 hours. The burned-back particles are then returned to the Soxhlet extractor for another two 24-hour extraction cycles in 16 M nitric acid.

The compact is received via pneumatic rabbit in Analytical Laboratory Hot Cell 1 and is transferred to Hot Cell 5 by a chain-driven cart that connects Cells 1–6. The compact is removed from the modified aluminum Swagelok bulkhead fitting that serves as a container and is weighed on the remote function balance in Cell 4. The weight is taken by placing the compact in a clean, tarred glass scintillation vial and transferring it to the balance for measurement.

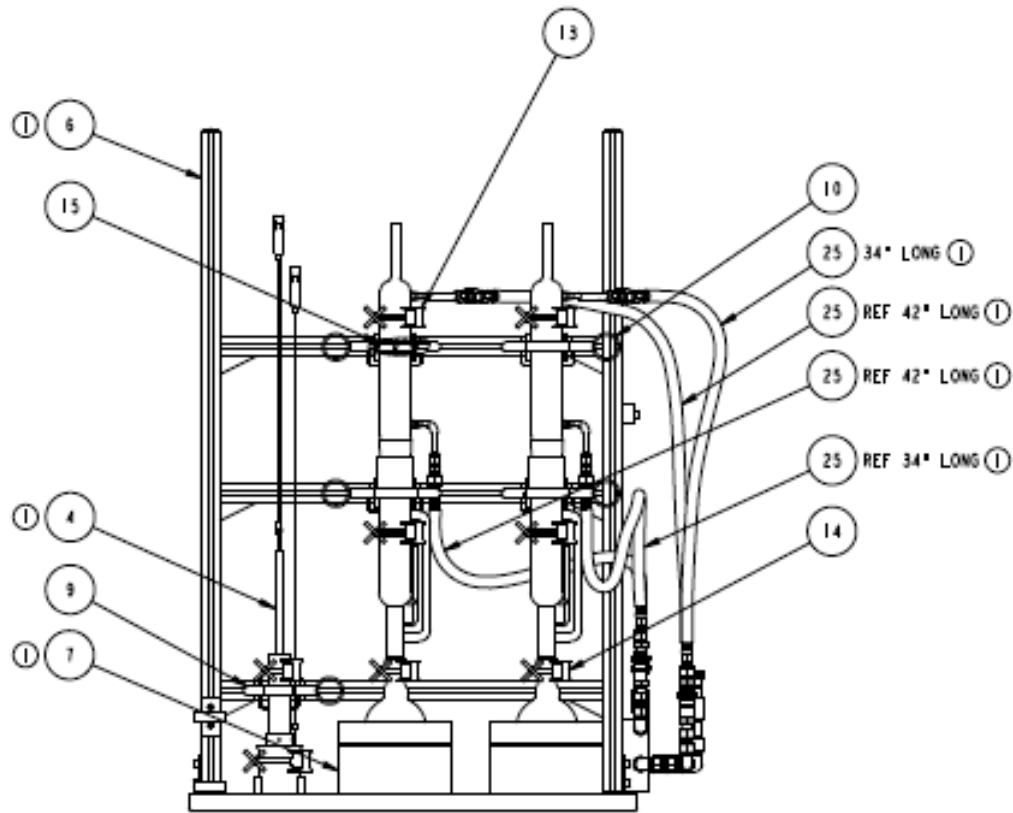
Once the compact weight is recorded, it is returned to Cell 5, where it is put into a clean, single-use deconsolidation tube. The entire deconsolidation setup is shown in Figure A-1. The deconsolidation tube is a 28-mm outer diameter glass tube that has a grating that supports the compact while the acid and applied electrical current break down the matrix. Based on experimentation during process development, it was concluded that a grating with 4-mm perforations allowed the particles to drop through with minimal plugging by the partially decomposed matrix. The deconsolidation tube fits loosely inside the Soxhlet thimble, which is a fused silica tube that has a porous No. 2 fused silica frit in the bottom that allows acid to flow through, but traps the majority of solids. The deconsolidation tube containing the compact is placed inside the thimble, which is in turn placed inside a glass tallform beaker. The two electrodes for the deconsolidation step are made of 20-gauge platinum-rhodium wire. The cathode is placed in the acid, either between the thimble and the deconsolidation tube, or between the thimble and the tallform beaker. The anode is a platinum-rhodium wire that has been threaded through a glass tube that is flared at the base to form an “elephant foot.” The anode wire is coiled at the bottom end to increase contact area where it sits on the compact. The beaker is filled with 4 M nitric acid to nearly the level of the bottom of the compact. The Tenma Model 72-6908 DC power supply is energized and the current set at 1 amp. Acid is added until current flow is established, and filled to cover approximately the bottom 1 mm of the compact. During system development and testing, it was determined that more coverage led to larger quantities of the matrix flaking off and partially plugging the perforated support in the deconsolidation tube. An open crossbar support test showed large pieces falling through before the matrix was uniformly broken down. The 4-mm perforated support was chosen as an effective compromise.



Figure A-1. Deconsolidation configuration.

The Soxhlet extractor system is composed of two standard glass units made in three sections: the boiling flask, situated in a heating mantle; the center section in which the thimble containing the specimen is located and condensate collects and periodically drains through siphon action; and the water cooled condenser located on top. Two units were installed in Cell 5 on the basis that it might be necessary to perform leach cycles in parallel. By procedure, the boiling flask is filled with 150 mL of concentrated nitric acid and placed in the heating mantle, the center section is inserted in the boiling pot and the thimble is placed inside the center section. The condenser is then attached and chilled water flow initiated. The chiller is installed outside the cell, at the rear, and maintains water temperature at 10°C with a flow of approximately 1 gallon per minute. The chiller is interlocked so that the heating mantles cannot be energized unless a minimum water flow is maintained. The acid vapor rises to the top, is condensed, and drains down to fill the volume containing the thimble. Periodically this volume fills to the level of a siphon tube that drains the collection volume back to the boiling flask. In this manner the specimen is continually flushed with freshly condensed acid solution. The assembly is shown in Figure A-2.

For heating, the Soxhlet boiling flasks are placed into electrical resistance mantles. The heating mantles are installed in Cell 5 and shown as item 7 in Figure A2. The heater is operator controlled and monitored outside the cell at the Cell 5 and 6 power control panel.



- I ASSEMBLY

Figure A-2. Framework with deconsolidation tube/vial (left) and two Soxhlet extractor stations.

The muffle furnace used for the burn-back phase is a Vulcan Model 3-55A bench top furnace, modified for installation in Hot Cell 5. An out-of-cell controller was fabricated in order to keep the electronics out of the radiation field. In this application, the furnace uses two 120-volt elements that are operated as individual heaters, departing from the manufacturer's configuration where the elements are wired in series and operated at 240 volts. In the manufacturer's arrangement, a failure of either heater element would disable the furnace. The manufacturer's data indicates that one heater element is capable of maintaining the oven at 750°C. Using the elements independently minimizes the need for heating element replacement in the event of failure. The furnace is equipped and controlled by a Type K thermocouple that is connected via the existing Hot Cell 5 Type K thermocouple wiring. An additional backup thermocouple has been installed in the furnace. The furnace is equipped with a door interlock switch and a fan. The door interlock switch deenergizes the heaters when the furnace door is not closed. The low voltage direct current fan is powered by the temperature controller.

Following the two pre-burn leach cycles, the Soxhlet thimble containing the particles is transferred to the muffle furnace. The furnace is heated to 750°C and held at this temperature for 72 hours. Air flow is maintained by adjusting the fan voltage on the external control panel to provide a detectable movement of the pinwheel mounted over the exhaust chimney. Once the desired duration is reached, the furnace is allowed to cool to <70°C and the thimble is returned to the Soxhlet extractor to perform the post-burn leaches.

The two post-burn leaching steps are performed with the same procedure described above for the pre-burn leaches. The particles are allowed to air dry in the thimble following completion of the final post-burn leach cycles. When dry, the particles are transferred to a metal storage container from which fractions are removed for particle inspection and selection.

The deconsolidation and two pre-burn leaches are expected to provide information on fission products that were external to the SiC layer and leached from the remaining matrix debris. These leach solutions would also provide information on any failed particles present in the compact, as the kernels would be exposed following deconsolidation and would be dissolved in the nitric acid solution. The post-burn leaches provide two basic pieces of information. If any particles are present with defective or otherwise failed SiC layers (cracked or porous SiC but intact pyrocarbon), the kernels will be exposed by the burning of intact pyrocarbon and dissolved in the nitric acid solution. As the burn step will also burn all of the remaining matrix debris as well as the OPyC layers, the post-burn leaches will also dissolve any fission products that remained in these components and could not be dissolved during the pre-burn leaches. In the absence of any particles with defective SiC, the total of all leach solutions should provide a total measure of fission products that were present outside of the SiC layers in the compact.

Appendix B

Particle Inspection and Irradiated Microsphere Gamma Analysis

Appendix B

Particle Inspection and Irradiated Microsphere Gamma Analysis

Following any of the deconsolidation-leach-burn-leach steps, particles can be visually inspected using a custom-designed optical macroscopy system. Individual particles can then be selected for specific purposes such as gamma spectrometry, burnup analysis, or microscopy. After completion of the second post-burn leach step, the particles are allowed to air dry and are then transferred from the thimble to a metal can for storage and handling. A fraction of the particles contained in the can (nominally 200 to 500 particles at a time) is transferred to an inspection dish, which is viewed on the shielded Leica macroscope that is installed in MFC Analytical Laboratory Hot Cell 5. The macroscope is connected to the control computer through a custom wall penetration that maintains shielding integrity.

A Leica Z16APO modular macroscope is oriented horizontally, viewing the sample array from below by a front surface mirror (Figures B-1 and B-2). The horizontal reflex configuration allows shielding to be installed to protect the camera. It also consumes the minimum working envelope. Viewing from below allows a clear overhead for particle manipulation and reduces interference with master slave manipulators. The Leica Z16 is equipped with an 8-megapixel DFC-490 CCD color camera that allows live video imaging at medium resolution and still image acquisition at high resolution. The unit is equipped with a 0.5x objective lens that allows a working distance of 187 mm, maximizing distance between the radiation source and the optics and electronics while minimizing the working envelope. The lens combination provides a 16:1 zoom capability that yields a field of view ranging from approximately 26 mm × 26 mm square to 1.6 mm × 1.6 mm, meaning that a maximum of ~1000 particles could be viewed at the minimum magnification of 9x, and 4 particles at the maximum of 144x. The digital image is communicated via a combination Firewire-Ethernet cable combination to the computer located outside the cell and displayed on the computer monitor. Images are captured and saved on the computer.

Particles placed on the optically flat glass inspection dish are viewed from below, which allows the selection needle to operate for picking up particles from above. Lighting is provided by two high-intensity variable light-emitting diodes that are mounted in pivot posts on the top of the microscope mirror box. This arrangement allows for some adjustment of shadow and highlight, but imperfect uniformity. When particles are placed on the inspection dish for viewing, the dish stage can be translated to view the dish and focus adjusted as needed. Newmark stepper motor-driven linear stages are used to position the viewing dish and vial tray platform in the x, y, and z directions as well as to raise and lower the vacuum needle during particle selection. The stages are controlled with joysticks that are able to achieve a nominal 0.2-mm precision of movement. Manual control using visual input from the microscope and through the cell window allows the operator to achieve consistent needle and visualization position, minimizing the need for electronic positioning tracking. Selected particles are picked up using a vacuum tweezer needle and photographed, then placed in glass V-vials for gamma spectrometry measurements. The needle stage moves up and down and can rotate the needle to allow a 360-degree view. Figure B-3 shows a particle attached to the vacuum needle.

Once particles have been selected from the inspection dish, they can be moved to individual Wheaton 0.3-mL V-vials, which are held in a rack on the inspection dish stage as shown in Figure B-2. Fifteen vials are arranged in the rack, which has an open bottom through which the V-vial can be viewed from below using the camera. The vacuum needle that is holding a particle is raised above rack height and the stage is positioned to align the needle with an open V-vial. The needle is then lowered into the mouth of the vial, the vacuum is shut off, and as the vacuum leaks off, the particle drops into the vial. This is confirmed visually by watching the microscope image on the computer screen.

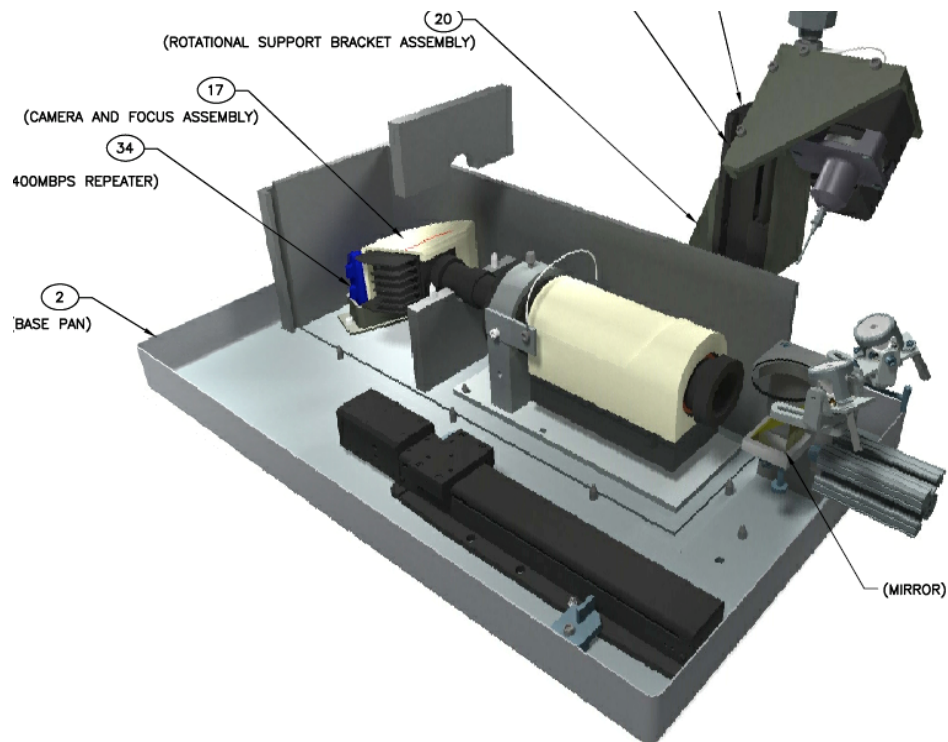


Figure B-1. Cutaway view of camera optical orientation without shielding

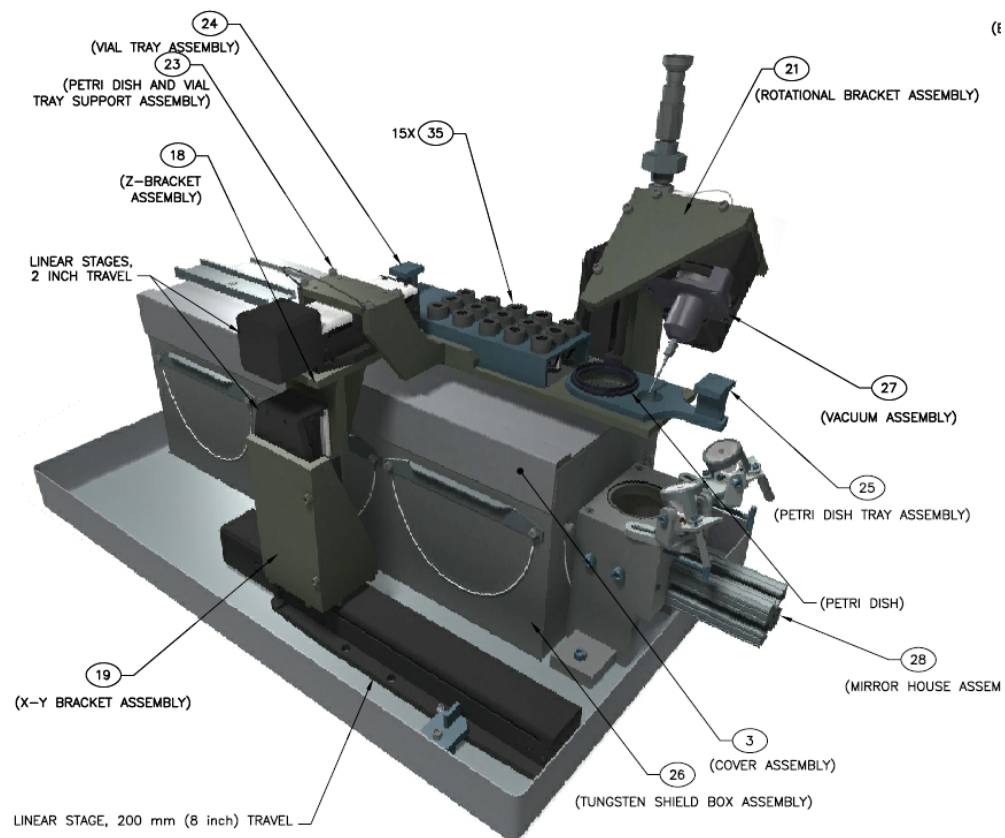


Figure B-2. Assembled isometric view of microscope stages and shielding

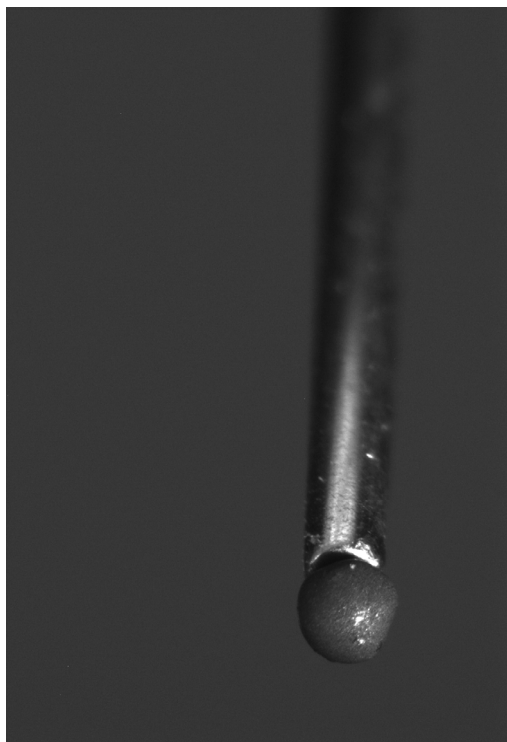


Figure B-3. Post deconsolidation particle viewed on the end of the vacuum tweezer needle.

Once particles have been selected and placed in the vials, the vials can be transferred to Analytical Laboratory Hot Cell 4, which is equipped with a gamma ray spectrometer that is located outside the hot cell, with gamma radiation transmitted through a port in the rear of the cell as shown in Figure B4.

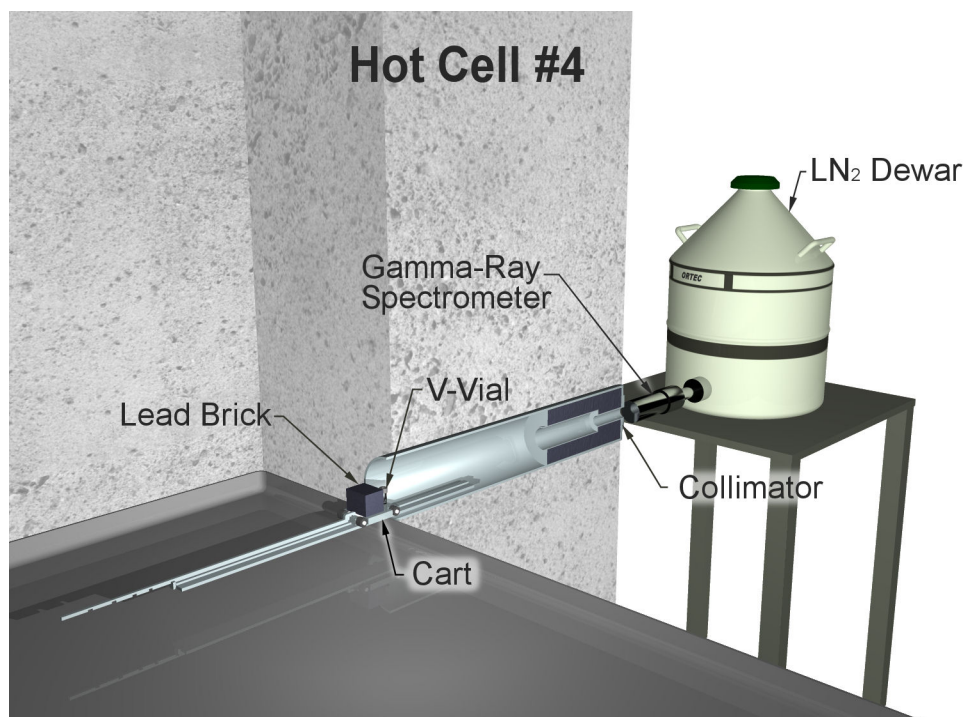


Figure B-4. MFC Analytical Laboratory Cell 4 spectrometer configuration.

The vial is positioned on the cart and moved to the position nearest the collimator to minimize the amount of background radiation from other sources inside the cell. The gamma spectrometer is an 18%-efficient Canberra germanium-lithium crystal that generates a signal that is parsed into specific energies by a Canberra Multi-Channel Analyzer and the spectrum is further analyzed using Apex software. The system is calibrated for particle measurement using a National Institute for Standards and Technology traceable Eu-152 source plated onto a polyethylene bead that approximates the size of a TRISO particle in a glass vial of the type used to hold the particles for counting.

The analysis in the Apex software quantifies any isotopes with measureable gamma emissions. The measured activity is based on a weighted average of all the detected gamma rays from a particular isotope, with weight given to the primary gamma-ray (typically the gamma ray with the highest branching ratio) and diminishing weight given to other gamma rays as their branching ratio decreases. Gamma rays with poor statistics or with known interferences are not used in the weighted average. Isotopes of particular interest include Ag-110m, Cs-134, Cs-137, Ce-144 (determined by measuring gamma emissions from Ce-144 and the daughter isotope Pr-144), Eu-154, Eu-155, Ru-106 (determined by measuring gamma emissions from the daughter isotope Rh-106). After the collected irradiated microsphere gamma analysis spectra were initially surveyed to identify which fission products were available for analysis, an AGR-1 specific library was created containing isotope, primary gamma energy, secondary gamma energy, and branching ratio. It included the isotopes of particular interest listed above. The default Apex library values for these isotopes were used with some notable exceptions. The primary gamma ray energy for Ag-110m was changed from 657 to 884 keV to alleviate difficulties in resolving the 657 keV Ag-110m gamma from the leading tail of the much more intense Cs-137 662 keV gamma. The other Ag-110m lines often had too few counts in the peak for quantification. In addition to the primary isotopes of interest, the activities of several other isotopes or their minimum detectable activities were reported including activation products Co-58, Co-60, Eu-152, and Mn-54, and fission products Zr-95 (and its Nb-95 daughter) and Ru-103.

Appendix C

Burnup Measurements

Appendix C

Burnup measurements

Burnup is calculated from ICP-MS measurements by using the measured mass of a specific fission product in the fuel, the cumulative fission yield of that specific fission product, and the total mass of actinides present in the sample. Ideally the fission products used in the calculations should have a small neutron absorption cross section, a high cumulative fission yield, and a similar fission yield for that isobar (same atomic number) between U and Pu fission. Chemically the fission product must also readily dissolve during the leaching process. Burnup determined from this process is defined as the percent of fissions that occurred in the fuel divided by the initial number of actinides or heavy metal present in the fuel (percent fissions per initial metal atom, or % FIMA). This technique uses the following formula to calculate burnup in % FIMA based on a specific fission product detected in the ICP-MS spectrum:

$$BU = \frac{\text{fissions}}{(\text{fissions} + \text{Actinides})} \times 100 = \frac{\left(\frac{N_{fp}}{y_{fp}} \right)}{\left(\left(\frac{N_{fp}}{y_{fp}} \right) + N_{Act} \right)} \times 100$$

where N_{fp} is number of atoms of a specific fission product fp measured in the sample, y_{fp} is the cumulative fission yield of fission product fp in the studied fuel, and N_{Act} is the number of atoms of actinides in the sample. In these measurements, all actinides with atomic numbers ranging from $A = 234$ to $A = 241$ were considered when calculating N_{Act} . In this formula, it is assumed that the initial actinides will either be destroyed by fission and create fission products or be transmuted into other actinide nuclei by neutron absorption reactions. This assumption allows the initial number of actinide atoms in the fuel (uranium in AGR-1) to be estimated by the number fissions that occur in the fuel plus the number of actinide atoms remaining in the fuel at the end of the experiment. Decay is ignored as a loss mechanism for the actinides. The decay of actinides often leads to other actinides (e.g., U-239 to Np-239 to Pu-239), or the half-life is sufficiently long (e.g. U-235 $t_{1/2} = 7.04 \times 10^8$ years) that the decay is insignificant as a loss mechanism over the course of the experiment.

For the AGR-1 experiment, most of the fission occurred in U-235, so it is reasonable as an estimate to use the U-235 cumulative fission yields (y_{fp}) for the various fission products. However detailed simulations of the AGR-1 experiment (J. W. Sterbentz, JMOCUP As-Run Daily Depletion Calculation for the AGR-1 Experiment in the ATR B-10 Position, ECAR-958 Rev. 1, August 2011) allow for the creation of effective cumulative fission product yields that are a weighted average of the different fission product yields based on the relative amount of fission that occurred in different actinides over the course of the experiment. The correction necessary because of effective fission product yield can be as much as 5% for some isotopes. In these calculations, the effective cumulative fission product yield was used instead of the U-235 fission product yield. Fission from the following actinides was considered for creating the effective fission yields: U-235, U-236, U-238, Pu-239, Pu-240, and Pu-241. The fission yields for each actinide were taken from ENDF/B-VII as found on the National Nuclear Data Center website (<http://www.nndc.bnl.gov/sigma/>)

There are six isotopes that work reliably well for the ICP-MS technique in the AGR-1 fuel: La-139, Ce-140, Ce-142, Pr-141, Nd-145, and Nd-146. These isotopes occur on the higher mass number peak of the bimodal fission product distribution. The differences between U-235 yield and Pu-239 yield are fairly small in this region as well. All of these isotopes are stable and have relatively small neutron absorption cross section with the exception of Nd-145. Because of its cross section the number of Nd-145 and Nd-146 atoms in the samples and their respective yields are usually summed in conducting a burnup

measurement. In this calculation the burnup measurement was found by taking the average result from Equation (1) for La-139, Ce-140, Ce-142, Pr-141, and the Nd-145/ Nd-146 combined result from Equation (1).

Appendix D

Ceramographic Morphology Classification

Appendix D

Ceramographic Morphology Classification

A comprehensive scheme for classifying AGR-1 particle morphologies was developed for analysis of cross-sectional particle images taken during ceramography of cross-sections from six irradiated AGR-1 fuel compacts.^a Several characteristic morphologies came to be recognized as these images were examined. The most common feature was a radial gap between the buffer and inner pyrolytic carbon (IPyC) layers where the buffer densified inward (outer surface moved toward kernel) during irradiation. In some particles with inward buffer densification the radial buffer-IPyC gap was interrupted by regions where the buffer stayed firmly bonded to the IPyC layer. Many of these particles debonded along most of the interface, while debonding was much less extensive on some other particles when the AGR-1 irradiation ended. The rarest case was where a particle had no buffer-IPyC gap. In these cases, the buffer stayed bonded to the IPyC layer around the entire circumference in the plane of the cross-section examined. The buffers in these particles still evidently densified, but the inner buffer surface moved radially outward rather than the outer buffer surface moving inward. Kernels in these particles often had larger pores than seen inside kernels within inwardly densified buffers.

The scheme for classifying irradiated AGR-1 particles by morphology in the plane of polish is presented with representative examples in Figure D-1. A radial buffer-IPyC gap around the entire circumference (completely detached buffer-IPyC interface) is designated as a Type A end-state morphology. Particles with fully bonded buffer and IPyC layers are termed Type B particles. Debonding along only part of the buffer-IPyC interface is called a Type AB morphology. Buffer fracturing occasionally occurred in Types A, B, and AB, which resulted in the six characteristic morphologies displayed in Figure D-1.

a Ploger, S.A., et al., *Ceramographic Examinations of Irradiated AGR-1 Fuel Compacts*, INL/EXT-12-25301, Rev. 1, September 2012.

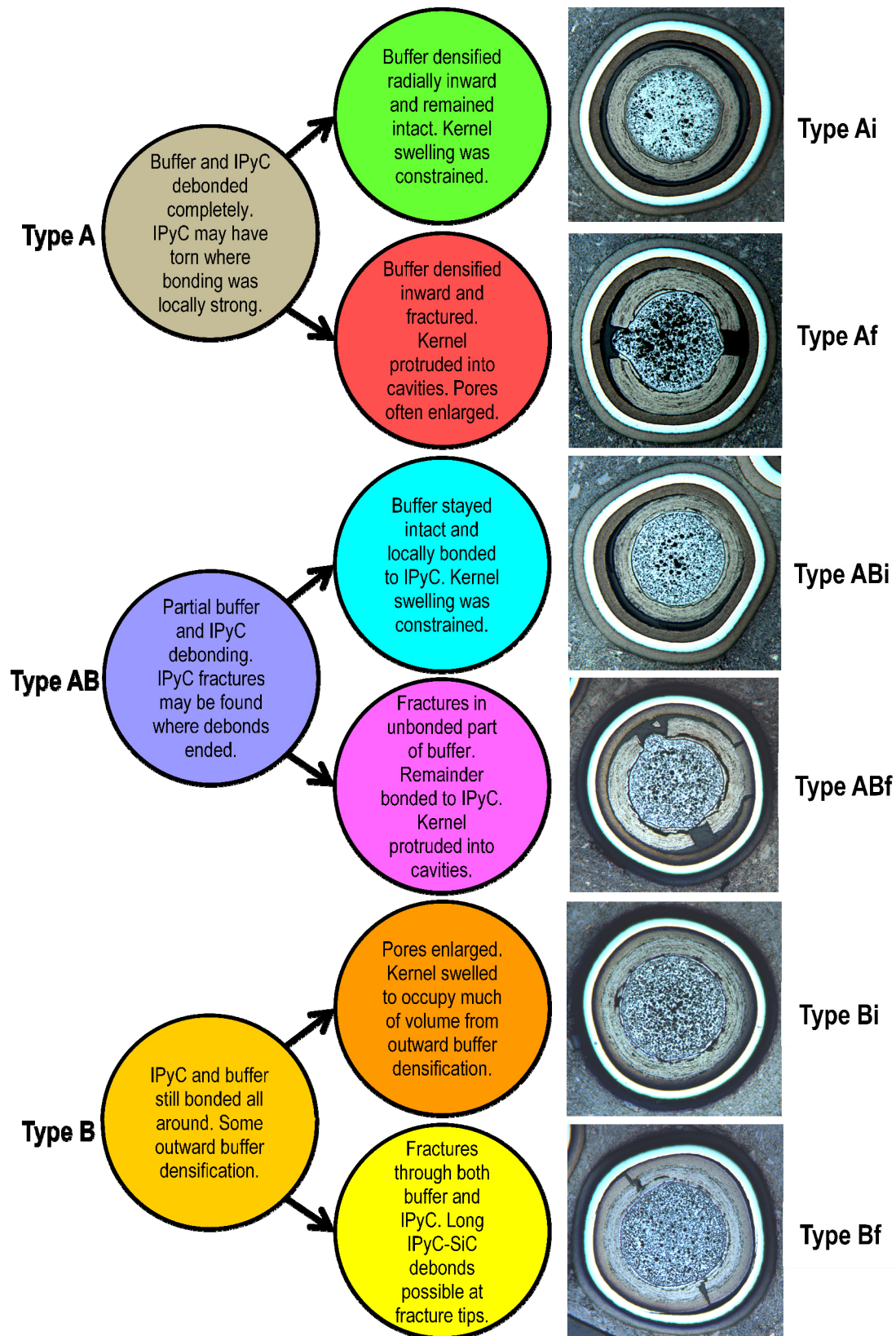


Figure D-1. Particle morphologies observed in AGR-1 fuel particle cross sections, where “i” denotes an intact buffer and “f” denotes a fractured buffer.